Separation and Purification Technology 390 (2026) 136908

Contents lists available at ScienceDirect

Separation and Purification Technology

journal homepage: www.elsevier.com/locate/seppur

Dual-functional *Z*-scheme $MgIn_2S_4/WO_3$ heterojunction for visible-light CO_2 reduction and antibiotic degradation: Unraveling charge transfer and reaction mechanisms

Yinghe Yang [a], Ali B.M. Ali [b], Shatha A. Aldaghfag [c], Haitao Lin [d,*], Hedi Elmonser [e,*], Ibrahm Mahariq [f,g,**], Bakhodir Saydullaev [h], Mukhtorjon Karimov [i], Miyribek Seytnazarov [j], Reda A. Haggam [k,*]

[a] Qujing University of Medicine &Health Sciences, Qujing, Yunnan 655100, China
[b] Advanced Technical College, University of Warith Al-Anbiyaa, Karbala, Iraq
[c] Department of Physics, College of Sciences, Princess Nourah bint Abdulrahman University, P. O. Box 84428, Riyadh 11671, Saudi Arabia
[d] Yuxi Normal University, Yunnan Province ZIP 653200, China
[e] Department of Mathematics, College of Science, Majmaah University, Al-Majmaah 11952, Saudi Arabia
[f] University College, Korea University, Seoul 02481, South Korea
[g] Department of Medical Research, China Medical University Hospital, China Medical University, Taichung, Taiwan
[h] The Department of Pharmaceutical and Chemistry, Alfraganus University, Yukori Karakamish Street 2a, Tashkent 100190, Uzbekistan
[i] Urgench State University, 14, Kh. Alimdjan Str, Urgench 220100, Uzbekistan
[j] Kimyo International University in Tashkent, Shota Rustaveli Str. 156, Tashkent 100121, Uzbekistan
[k] Department of Chemistry, Faculty of Science, Islamic University of Madinah, Madinah 42351, Saudi Arabia

ARTICLE INFO

Keywords:
Heterojunction photocatalyst
CO_2 reduction
Water treatment
Tetracycline
RSM
DFT calculations

ABSTRACT

The escalating crises of antibiotic pollution and atmospheric CO_2 demand advanced technologies capable of simultaneous environmental remediation and renewable fuel production. Herein, we report the rational design and fabrication of a direct *Z*-scheme $MgIn_2S_4/WO_3$ heterojunction via a controlled hydrothermal–ultrasonication method for concurrent Tetracycline (TC) degradation and CO_2 photoreduction under visible-light irradiation. The heterostructure, comprising flower-like $MgIn_2S_4$ nanostructures intimately coupled with WO_3 nanoparticles, exhibits enhanced light absorption, interfacial charge separation, and redox potential alignment. Comprehensive characterization confirmed the successful construction of a *Z*-scheme charge-transfer pathway that retains strongly reducing electrons in $MgIn_2S_4$ ($E_{CB} = -0.65$ eV) and highly oxidizing holes in WO_3 ($E_{VB} = +3.14$ eV), essential for driving both reduction and oxidation reactions. Simultaneously, CO_2 photoreduction yielded 35.27 μmol g^{-1} h^{-1} CH_4 and 18.01 μmol g^{-1} h^{-1} CO, representing enhancements of up to 32- and 11-fold over pure WO_3, and 10- and 4-fold over $MgIn_2S_4$. RSM–CCD optimization validated the statistical reliability of the photocatalytic process ($R^2 = 0.9980$; adj-$R^2 = 0.9960$; pred-$R^2 = 0.9902$) and identified the optimum conditions, under which the composite achieved a superior TC degradation efficiency of 97.69%—representing a 1.9-fold and 2.2-fold enhancement over pristine $MgIn_2S_4$ and WO_3, respectively—along with 81.16% TOC mineralization. The catalyst showed exceptional versatility, degrading various antibiotics with high efficiency and robust performance across different real water samples. It retained 87.76% activity after four cycles, confirming outstanding stability. Mechanistic insights supported by ESR and DFT analyses revealed that $\bullet O_2^-$ and •OH radicals dominate the reaction pathway, while toxicity modeling indicated that all degradation intermediates exhibited significantly lower acute and mutagenic toxicity than TC itself. This work establishes the $MgIn_2S_4/WO_3$ *Z*-scheme heterojunction as a robust, durable and versatile photocatalyst, providing a mechanistic blueprint for integrated environmental remediation and solar fuel production.

* Corresponding authors.
** Corresponding author at: University College, Korea University, Seoul 02481, South Korea.
E-mail addresses: drhtlin@yxnu.edu.cn (H. Lin), h.elmonser@mu.edu.sa (H. Elmonser), lbmmahariq@gmail.com (I. Mahariq), relhaggan@iu.edu.sa (R.A. Haggam).

https://doi.org/10.1016/j.seppur.2026.136908
Received 24 November 2025; Received in revised form 24 December 2025; Accepted 14 January 2026
Available online 15 January 2026
1383-5866/

1. Introduction

The escalating atmospheric carbon dioxide (CO_2) concentration, primarily driven by intensive fossil fuel consumption and industrial activities, represents a paramount environmental challenge of the 21st century [1–3]. As a principal greenhouse gas, CO_2 is a major contributor to global warming, ocean acidification, and climate instability, thereby jeopardizing global ecosystems and sustainable development [4]. Addressing this crisis necessitates innovative strategies that not only mitigate emissions but also convert this abundant C1 feedstock into value-added solar fuels, such as carbon monoxide (CO), methane (CH_4), and methanol (CH_3OH) [5,6]. Concurrently, the pervasive contamination of water resources by pharmaceuticals—particularly antibiotics—poses a parallel threat to environmental and public health [7]. Global antibiotic consumption exceeds 200,000 t annually, with TC ranking among the most widely used broad-spectrum agents in human therapy, veterinary medicine, and aquaculture [8]. Due to its incomplete metabolism, approximately 75% of administered TC is excreted in active forms, leading to its persistent detection from ng L^{-1} to μg L^{-1} in diverse water matrices. The inherent stability and recalcitrance of TC facilitate its environmental persistence, bioaccumulation, and promotion of antibiotic resistance genes (ARGs), presenting serious ecological and toxicological risks [9]. The convergence of these dual challenges rising CO_2 levels and persistent antibiotic pollution underscores an urgent need for advanced photocatalytic systems capable of simultaneous CO_2 conversion into sustainable fuels and oxidative degradation of pharmaceutical pollutants, thereby contributing to integrated environmental remediation and a carbon-neutral future.

Conventional treatment methods such as ozonation, adsorption [10], and membrane filtration [11,12] show limited effectiveness for tetracycline removal because they often suffer from incomplete mineralization, high operating costs, and possible formation of toxic by-products [13–15]. In addition, biological treatment typically provides low removal efficiency (<30%) and requires long processing times [16,17]. These limitations motivate the development of advanced oxidation processes (AOPs), among which semiconductor photocatalysis is particularly attractive because it harnesses solar energy to generate electron–hole pairs that drive redox reactions under mild conditions, enabling pollutant degradation and CO_2 conversion to value-added fuels [18,19]. Nonetheless, single-component photocatalysts remain hindered by rapid charge recombination, insufficient visible-light utilization, and inadequate redox potentials, making heterostructure engineering essential to enhance charge separation while preserving strong redox capability for efficient dual-functional photocatalysis.

Single-component photocatalysts are limited by fast recombination, poor visible-light utilization, and insufficient redox power. Heterojunctions can promote charge separation via interfacial electric fields, but type-II systems often weaken redox ability, and S-schemes may still suffer interfacial recombination [20]. By contrast, *Z*-scheme heterojunctions selectively recombine low-energy carriers and retain the strongest electrons and holes on different components, making them well suited for coupled CO_2 reduction and pollutant degradation. Recent literature has demonstrated that *Z*-scheme-based heterojunctions can markedly enhance visible-light degradation of emerging contaminants, most commonly by pairing $MgIn_2S_4$ with carbon nitride platforms. For instance, Liu et al. constructed a 3D/2D $MgIn_2S_4/g\text{-}C_3N_4$ *Z*-scheme for ranitidine removal, achieving rapid kinetics and notable tolerance toward environmental variations; the improvement was ascribed to strengthened charge separation, preserved redox capability, and increased light utilization enabled by the hierarchical morphology [21]. Beyond pollutant-only systems, multifunctional *Z*-scheme designs have also been reported. Abdallah et al. developed a $Ce_2Sn_2O_7$–SiW_9Co_3 heterojunction with charge transfer switched toward a Z-scheme pathway, enabling simultaneous H_2 evolution and TC degradation, supported by ESR/scavenger tests and LC–MS pathway/toxicity analyses [22]. More recently, Yang et al. reported a Ti_3C_2 MXene-based direct Z-scheme nanocomposite ($Bi_2O_3/Ag_3PO_4@Ti_3C_2$) for coupled antibiotic removal and CO_2 photoreduction, integrating process optimization and DFT-assisted pathway interpretation [23]. Collectively, these studies highlight the field's progress toward high-efficiency charge management and multifunctionality under visible light. Despite these advances, a key challenge remains: simultaneously maintaining strong oxidation power for deep antibiotic mineralization while preserving strong reduction ability for CO_2 activation within a simple and stable heterojunction architecture. In many $MgIn_2S_4/g\text{-}C_3N_4$ systems, the "oxidation side" is not intrinsically optimized for sustaining highly oxidative holes required for robust •OH generation and deep oxidation, particularly under complex real-water matrices, whereas some multifunctional systems rely on more compositionally complex components (e.g., polyoxometalate clusters or MXene-assisted multi-interfaces). In this context, introducing WO_3 as an oxidation-oriented counterpart provides a rational route to reinforce the oxidative branch of the *Z*-scheme, because WO_3 is widely recognized for its highly positive valence-band potential and strong hole-driven oxidation capacity. Therefore, constructing a direct *Z*-scheme $MgIn_2S_4/WO_3$ interface is expected to offer a clearer redox-complementary advantage: strongly reducing electrons retained on $MgIn_2S_4$ to drive CO_2 reduction, coupled with strongly oxidizing holes retained on WO_3 to promote antibiotic oxidation/mineralization, thereby aligning the material design more directly with the requirements of dual-functional photocatalysis.

Herein, we report the rational construction of a direct Z-scheme $MgIn_2S_4/WO_3$ heterojunction via a tailored hydrothermal–ultrasonication strategy to promote intimate interfacial coupling and efficient charge transport. The resulting architecture enables dual-functional visible-light photocatalysis, integrating tetracycline degradation with CO_2 photoreduction to solar fuels. Comprehensive characterizations were performed to correlate material properties with catalytic performance, while the charge-transfer mechanism and reaction chemistry were clarified through scavenger/ESR analyses and DFT calculations. Practical relevance was further substantiated by cycling stability, TOC mineralization, toxicity prediction of intermediates, and performance validation in real-water matrices and across multiple antibiotic classes. Overall, this work establishes $MgIn_2S_4/WO_3$ as a robust *Z*-scheme platform and offers mechanistic and design insights for next-generation multifunctional photocatalysts toward coupled carbon valorization and wastewater remediation.

2. Methodology

2.1. Reagents

All chemicals were of analytical grade and were used as received, without additional purification (e.g., no recrystallization or further distillation), unless otherwise specified. Magnesium chloride hexahydrate ($MgCl_2{\cdot}6H_2O$), indium(III) chloride tetrahydrate ($InCl_3{\cdot}4H_2O$), and thioacetamide (TAA) were purchased from Merck and used as the Mg, In, and S precursors, respectively, for the synthesis of $MgIn_2S_4$. Sodium tungstate dihydrate ($Na_2WO_4{\cdot}2H_2O$), sodium chloride (NaCl), and hydrochloric acid (HCl, 37%) were employed for the preparation of WO_3. Ethylene glycol (EG) served as the reaction solvent and complexing medium during $MgIn_2S_4$ synthesis, while deionized water and anhydrous ethanol were used for washing and dispersion steps. Tetracycline hydrochloride (TC, $C_{22}H_{24}N_2O_8{\cdot}HCl$, ≥98%, Sigma-Aldrich) was used as the target contaminant without further purification. Ultra-high-purity CO_2 (99.999%) and high-purity N_2 (99.99%) gases were supplied by Air Products. All aqueous solutions were prepared using freshly deionized water (resistivity ≥18.2 MΩ·cm) produced by a Milli-Q purification system.

2.2. Synthesis of $MgIn_2S_4$

Nano-flower-like $MgIn_2S_4$ was prepared via a hydrothermal route. In

a typical synthesis, 0.10165 g of $MgCl_2·6H_2O$ and 0.29324 g of $InCl_3·4H_2O$ were dissolved in 70 mL of ethylene glycol under constant stirring until a transparent solution was obtained (Fig. 1a). Subsequently, 0.30052 g of thioacetamide was added as the sulfur source, and the mixture was stirred magnetically for 30 min to ensure complete homogenization. The resulting solution was transferred into a 100 mL Teflon-lined stainless-steel autoclave and maintained at 180 °C for 12 h. After natural cooling to ambient temperature, the yellow precipitate was collected by centrifugation, repeatedly rinsed with deionized water and anhydrous ethanol to remove residual ions, and dried under vacuum at 60 °C for 12 h. The obtained yellow powder was denoted as $MgIn_2S_4$.

2.3. Synthesis of WO_3

WO_3 nanoparticles were synthesized through a straightforward hydrothermal process. Briefly, 1 g (0.1 M) of $Na_2WO_4·2H_2O$ was dissolved in 50 mL of deionized water under magnetic stirring until complete dissolution occurred (Fig. 1a). Next, 0.30 g of NaCl was added to regulate the ionic strength of the medium, followed by pH adjustment to 2.0 using diluted HCl (1 M) under continuous stirring. After 30 min of mixing, the solution was transferred to an 80 mL Teflon-lined stainless-steel autoclave and heated at 180 °C for 18 h. The obtained precipitate was filtered, thoroughly washed with deionized water and ethanol, and finally dried at 70 °C for 3 h to yield pure WO_3 powder.

2.4. Synthesis of Z-scheme $MgIn_2S_4/WO_3$

The Z-scheme $MgIn_2S_4/WO_3$ composites were prepared by a facile aqueous dispersion–ultrasonication strategy (Fig. 1b). A known amount of $MgIn_2S_4$ powder was dispersed in 150 mL of deionized water and magnetically stirred for 20 min to form a homogeneous suspension. Then, pre-synthesized WO_3 nanoparticles were added in varying mass fractions (5, 15, 25, and 35 wt% relative to WO_3) to tailor the interfacial composition. The mixtures were stirred in the dark for 20 min, followed by ultrasonication for 40 min to enhance the contact between $MgIn_2S_4$ and WO_3 and facilitate the formation of a direct *Z*-scheme junction. Finally, each dispersion was stirred for an additional 30 min, filtered, and vacuum-dried at 80 °C overnight. The resulting composites were denoted as x- $MgIn_2S_4/WO_3$ (x = 5, 15, 25, and 35 wt%).

2.5. Photocatalytic tetracycline degradation and RSM-CCD optimization; 2.6. Photocatalytic CO_2 conversion experiments; 2.7. Density functional theory (DFT) calculations and 2.8. Characterization techniques

Details of these sections are provided in the Supplementary Information file.

3. Results and discussion

3.1. Morphological, textural and structural properties

The surface morphology and microstructural features of the synthesized samples were examined by field-emission scanning electron microscopy (FE-SEM) and transmission electron microscopy (TEM), as presented in Fig. 2**(a–e)**. The pristine WO_3 (Fig. 2a) exhibits an irregularly aggregated particulate structure composed of nearly spherical nanoparticles with dimensions typically below 1 μm. The particles are closely packed with moderate surface roughness, providing multiple active sites that can favor charge separation and surface reactions. This morphology is consistent with hydrothermally prepared WO_3 reported

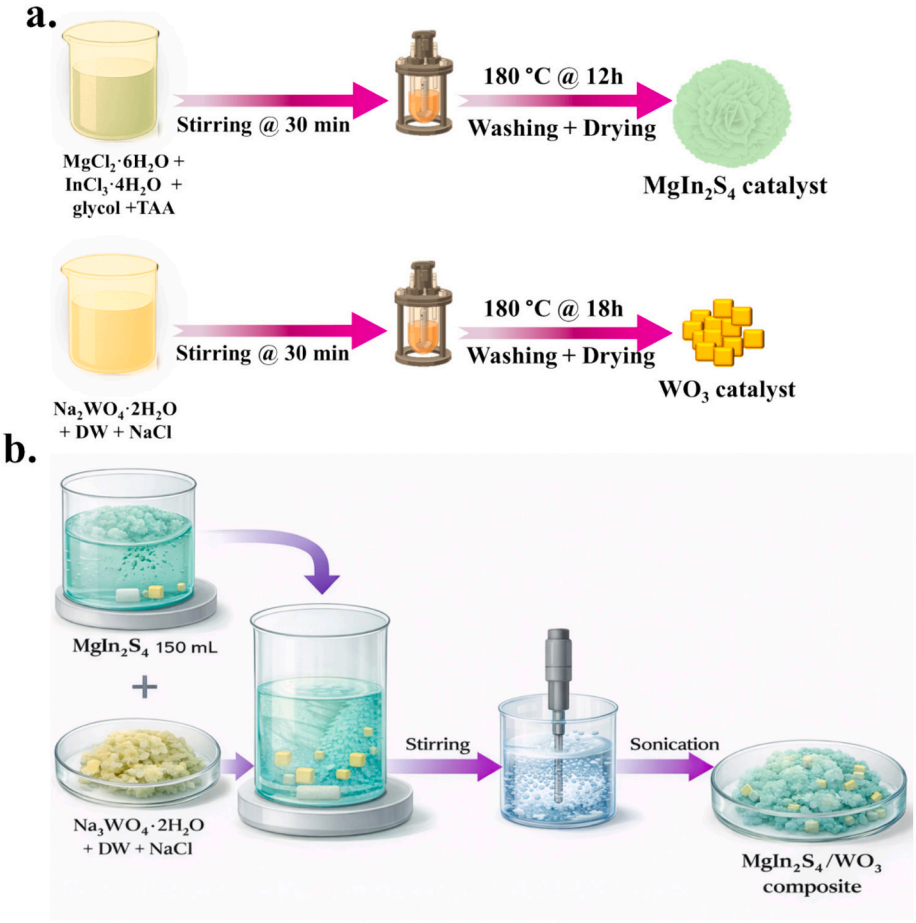

Fig. 1. Schematic of the synthesis of photocatalyst.

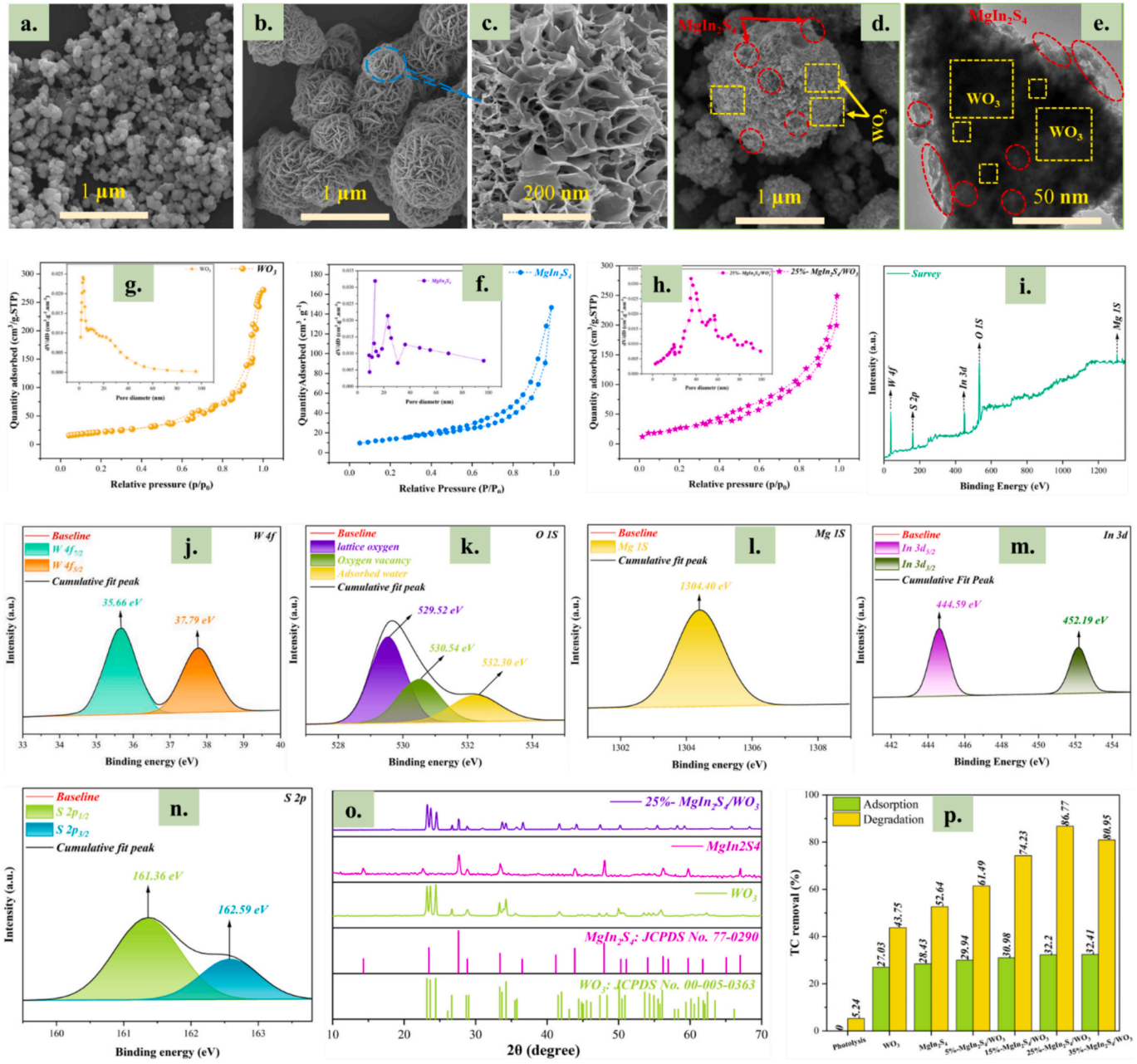

Fig. 2. Comprehensive characterization of the synthesized photocatalysts: (a) WO_3 nanoparticles; (b, c) $MgIn_2S_4$ nanoflowers; (d, e) SEM and TEM images of the 25 wt% $MgIn_2S_4/WO_3$ composite showing uniform WO_3 distribution. (f–h) N_2 adsorption–desorption isotherms of $MgIn_2S_4$, WO_3, and 25 wt% $MgIn_2S_4/WO_3$. (i–n) XPS survey and high-resolution spectra (W 4f, O 1 s, Mg 1 s, In 3d, S 2p) confirming the chemical states and oxygen vacancies. (o) XRD patterns verifying the coexistence of crystalline WO_3 and $MgIn_2S_4$ phases. (p) TC removal efficiencies, highlighting the superior performance of 25 wt% $MgIn_2S_4/WO_3$.

in earlier studies, confirming the successful nucleation and crystal growth under the employed synthesis conditions [24].

In contrast, the pure $MgIn_2S_4$ (Fig. 2b and c) demonstrates a distinct flower-like hierarchical structure constructed from ultrathin nanosheets radiating from a central core. The uniform nanoflowers, approximately 1–2 μm in diameter, exhibit well-defined petal-like architectures with porous interspaces that can facilitate light scattering and enhance the diffusion of reactant molecules. The high-magnification image (Fig. 2c) reveals that the nanosheets are only a few tens of nanometers thick, forming an open framework advantageous for both photon capture and charge transport. Such a three-dimensional assembly derived from the controlled hydrothermal reaction provides a large specific surface area and efficient electron migration pathways, essential for high photocatalytic activity [25]. Upon coupling $MgIn_2S_4$ with WO_3 to construct the *Z*-scheme heterojunction (Fig. 2d and e), a pronounced morphological transformation is observed. The optimized 25 wt% $MgIn_2S_4/WO_3$ composite (Fig. 2d) retains the general spherical outline of $MgIn_2S_4$ nanoflowers but displays numerous fine WO_3 nanoparticles uniformly distributed over their surfaces. The tight interfacial adhesion between WO_3 and $MgIn_2S_4$ ensures intimate contact, enabling the direct formation of a heterojunction that promotes bidirectional charge transfer across the interface. This well-anchored configuration minimizes particle agglomeration and facilitates rapid photogenerated electron migration, suppressing recombination losses. Further insights from the TEM micrograph (Fig. 2e) corroborate the SEM observations. The dark contrast regions correspond to the $MgIn_2S_4$ matrix, while the lighter crystalline domains represent WO_3 nanoparticles that are well-dispersed within the composite. The close contact between both phases indicates a

coherent interface, which is crucial for constructing an efficient *Z*-scheme charge-transfer pathway [26]. The nanoscale integration of WO_3 onto the $MgIn_2S_4$ surface not only extends visible-light absorption but also enhances the redox potential difference between the two semiconductors. Collectively, these morphological observations confirm that the designed synthetic strategy successfully yields a robust, well-interfaced $MgIn_2S_4/WO_3$ heterostructure with high structural integrity and abundant active sites, forming a strong foundation for the dual-functional photocatalytic performance discussed in subsequent sections.

The specific surface area, pore volume, and pore diameter of the synthesized photocatalysts were evaluated through nitrogen adsorption–desorption isotherms (Figs. 2f–2h), and the corresponding parameters are summarized in **Table S1**. All samples exhibited type IV isotherms with distinct H_3-type hysteresis loops, confirming the presence of mesoporous structures derived from aggregated nanoparticles and nanosheets. Such porosity facilitates efficient molecular diffusion and provides abundant accessible surface sites for photocatalytic reactions. The pristine WO_3 (Fig. 2f) displays a typical mesoporous profile with a BET surface area of 24.1 $m^2\ g^{-1}$, an average pore diameter of 11.8 nm, and a total pore volume of 0.019 $cm^3\ g^{-1}$. This relatively moderate surface area arises from the dense nanoparticle aggregation observed in its SEM image, which restricts gas adsorption to external surface regions. The $MgIn_2S_4$ nanoflowers (Fig. 2g), in contrast, show a lower surface area (11.3 $m^2\ g^{-1}$) but slightly larger pores (17.1 nm) due to the three-dimensional sheet-assembled morphology. The loose arrangement of ultrathin nanosheets produces hierarchical porosity with interparticle voids that enhance gas diffusion; however, the limited number of micropores contributes to the overall lower surface area.

A marked improvement in textural properties was achieved after coupling $MgIn_2S_4$ with WO_3. The BET surface area increased progressively with increasing WO_3 loading—from 38.6 $m^2\ g^{-1}$ for the 5 wt% composite to 71.9 $m^2\ g^{-1}$ for the 25 wt% sample—alongside corresponding rises in pore volume (0.025 to 0.037 $cm^3\ g^{-1}$) and mean pore diameter (18.4 to 21.5 nm). The enhanced porosity and surface area can be attributed to the homogeneous dispersion of WO_3 nanoparticles over the $MgIn_2S_4$ nanosheet surface, which prevents the restacking of the sulfide layers and generates new interfacial pores. The composite thus provides more active adsorption sites and facilitates the interfacial charge transfer essential for efficient photocatalysis [27]. The 25 wt% $MgIn_2S_4/WO_3$ sample (Fig. 2h) exhibited the highest specific surface area and pore volume, confirming that this composition achieves an optimal balance between structural openness and particle connectivity. At higher loading (35 wt%), the BET area slightly decreased to 64.4 $m^2\ g^{-1}$, implying that excess WO_3 begins to occupy and block the mesopores of $MgIn_2S_4$, thereby reducing the accessible surface region. The BJH pore-size distribution curves (insets of Figs. 2f–2h) further verify a dominant mesoporous regime (10–30 nm), consistent with hierarchical architectures suitable for light-driven catalytic reactions.

The surface composition and oxidation states of the optimized 25%–$MgIn_2S_4/WO_3$ heterojunction were examined by X-ray photoelectron spectroscopy (XPS), and the corresponding spectra are displayed in Figs. 2**(i–n)**. The full survey spectrum (Fig. 2i) confirms the coexistence of Mg, In, S, W, and O elements, validating the successful formation of the hybrid composite without any detectable impurities or secondary phases. The presence of O 1 s in addition to W 4f signals signifies the existence of oxygenated tungsten species, while Mg 1 s, In 3d, and S 2p peaks are characteristic of the $MgIn_2S_4$ lattice. The high-resolution spectrum of W 4f (Fig. 2j) shows two prominent peaks centered at 35.66 eV and 37.79 eV, corresponding respectively to W $4f_{7/2}$ and W $4f_{5/2}$ of W^{6+} in stoichiometric WO_3 [28]. The absence of additional peaks at lower binding energies rules out the presence of reduced tungsten species (W^{5+} or W^{4+}), implying a well-crystallized oxide phase with stable electronic configuration. These results indicate that WO_3 retains its oxidation state after heterojunction formation, acting as a robust electron acceptor in the *Z*-scheme charge-transfer system. The O 1 s spectrum (Fig. 2k) can be deconvoluted into three distinct components at 529.52 eV, 530.54 eV, and 532.30 eV, assigned to lattice oxygen (O^{2-} bound to W), oxygen vacancies (defective O sites), and surface-adsorbed oxygen or hydroxyl species, respectively [29,30]. The notable intensity of the middle component (oxygen vacancy) suggests that defect states are abundant at the $MgIn_2S_4/WO_3$ interface, which can promote visible-light absorption and act as shallow traps for photoinduced electrons, effectively facilitating charge separation and enhancing redox kinetics. The Mg 1 s core-level spectrum (Fig. 2l) exhibits a single symmetric peak at 1304.40 eV, characteristic of Mg^{2+} in the $MgIn_2S_4$ spinel structure. The absence of any satellite peaks confirms the chemical stability of the Mg environment and the absence of oxide or hydroxide impurities [31]. The In 3d region (Fig. 2m) displays two sharp peaks located at 444.59 eV (In $3d_{5/2}$) and 452.19 eV (In $3d_{3/2}$), which correspond to In^{3+} species coordinated with sulfur atoms [32]. These positions are in good agreement with standard $MgIn_2S_4$ references, signifying that indium preserves its valence state within the sulfide lattice upon hybridization. The S 2p spectrum (Fig. 2n) is composed of two peaks at 161.36 eV (S $2p_{3/2}$) and 162.59 eV (S $2p_{1/2}$), confirming the divalent sulfide state (S^{2-}) in $MgIn_2S_4$ [33,34]. The absence of peaks above 164 eV excludes the formation of oxidized sulfur species such as SO_4^{2-}, demonstrating that the sulfide framework remains intact after compositing with WO_3.

The crystalline phases and structural purity of the synthesized samples were examined by X-ray diffraction (XRD), and the corresponding diffraction patterns are illustrated in Fig. 2o. The pristine WO_3 exhibits distinct peaks located at $2\theta = 23.1°$, 23.6°, 24.4°, 26.6°, 28.8°, 33.3°, 34.1°, 41.7°, 49.9°, and 55.7°, which correspond to the (002), (020), (200), (120), (112), (022), (202), (222), (312), and (224) crystallographic planes, respectively. These reflections match well with the monoclinic phase of WO_3 (JCPDS No. 00–005-0363), confirming that the hydrothermal synthesis yielded phase-pure, well-crystallized tungsten trioxide [35]. The XRD pattern of $MgIn_2S_4$ displays characteristic diffraction peaks at $2\theta = 26.5°$, 30.3°, 38.5°, 47.4°, 51.3°, and 55.9°, corresponding to the (220), (311), (400), (511), (440), and (533) planes, respectively, in excellent agreement with the cubic spinel structure of $MgIn_2S_4$ (JCPDS No. 77–0290) [36]. The relatively sharp and intense reflections indicate good crystallinity, while the absence of extraneous peaks confirms the formation of a single-phase ternary sulfide without secondary MgS or In_2S_3 impurities. For the 25 wt% $MgIn_2S_4/WO_3$ composite, the diffraction pattern exhibits the combined reflections of both parent semiconductors. The major peaks of $MgIn_2S_4$ are preserved, whereas the characteristic peaks of WO_3 can be distinctly identified at 2θ: 23.1° and 24.4°, indicating successful integration of both crystalline phases. No additional or shifted peaks are observed, suggesting that the two components are physically coupled rather than forming a new alloyed or doped phase. However, a slight attenuation in the intensity of WO_3 peaks and broadening of $MgIn_2S_4$ reflections can be observed, which can be attributed to nanoscale interfacial interaction and partial coverage of WO_3 nanoparticles on the $MgIn_2S_4$ surface. The coexistence of both sets of diffraction peaks in the composite confirms the formation of a heterojunction interface without structural distortion.

3.2. Optimization of synthesized photocatalysts and photocatalytic CO_2 conversion to solar fuels

The photocatalytic activity of the synthesized samples was evaluated through the degradation of TC under visible-light irradiation, and the comparative performance results are presented in Fig. 2p. The negligible degradation efficiency of TC under direct photolysis (5.24%) confirms that self-photodecomposition is insignificant without the assistance of a photocatalyst. When using pristine WO_3, the TC removal reached only 43.75%, attributable to its moderate bandgap (2.76 eV) and relatively positive conduction band (+0.38 eV), which limit the generation of sufficiently reducing electrons for efficient pollutant degradation [37]. Although WO_3 exhibits good oxidation capability owing to its deep valence band (3.14 eV), the rapid electron–hole recombination, as revealed by its weak PL quenching and moderate BET surface area (24.1

$m^2\ g^{-1}$), suppresses overall photocatalytic performance. In contrast, pure $MgIn_2S_4$ achieved a slightly higher degradation efficiency of 52.04%, benefiting from its narrower bandgap (2.13 eV) and more negative conduction band potential (−0.65 eV), which enable stronger photoreduction ability. Its hierarchical flower-like structure, composed of ultrathin nanosheets with mesoporous interspaces, further enhances light scattering and molecular adsorption. However, the recombination of photoinduced carriers within $MgIn_2S_4$ still restricts its activity, as confirmed by its low surface area (11.3 $m^2\ g^{-1}$) and the absence of defect-mediated electron trapping centers seen in WO_3 [38].

The $MgIn_2S_4/WO_3$ composites exhibited a remarkable improvement in TC degradation efficiency, confirming the successful formation of a synergistic heterojunction interface that promotes charge separation. The photocatalytic performance increased progressively with WO_3 loading—from 61.49% for 5 wt% WO_3 to 74.23% for 15 wt% WO_3—and reached a maximum of 86.77% for the 25 wt% $MgIn_2S_4/WO_3$ composite. Beyond this optimum ratio, a slight decrease to 80.95% was observed at 35 wt%, primarily due to excessive WO_3 nanoparticles covering the active surface of $MgIn_2S_4$, leading to partial blockage of active sites and light-shielding effects. This optimal photocatalytic performance of the 25 wt% $MgIn_2S_4/WO_3$ heterostructure can be rationalized by its superior physicochemical features. The BET analysis revealed that this sample possesses the largest specific surface area (71.9 $m^2\ g^{-1}$) and pore volume (0.037 $cm^3\ g^{-1}$), providing abundant adsorption and reaction sites. XPS analysis confirmed the coexistence of Mg^{2+}, In^{3+}, S^{2-}, W^{6+}, and oxygen vacancies, which serve as shallow charge traps and facilitate visible-light absorption. The XRD results demonstrated the intact crystalline nature of both semiconductors, ensuring efficient interfacial contact for charge migration [39]. Furthermore, SEM and TEM analyses revealed intimate anchoring of WO_3 nanoparticles on the $MgIn_2S_4$ nanosheets, forming a continuous *Z*-scheme junction that accelerates interfacial charge transfer.

The photocatalytic CO_2 reduction performance of the synthesized materials was evaluated under visible-light irradiation to assess their capability for solar fuel generation, as presented in Figs. 3(a–c). The principal carbon-containing products identified were CO and CH_4, both of which are valuable chemical fuels formed through multi-electron reduction pathways. The absence of other carbonaceous species (e.g., methanol, formate) confirmed high product selectivity toward these two reduction products. As shown in Fig. 3a, the pristine WO_3 exhibited limited CO_2 reduction activity, producing only 1.09 μmol $g^{-1}\ h^{-1}$ of CH_4 and 1.53 μmol $g^{-1}\ h^{-1}$ of CO. This poor performance arises from WO_3's wide bandgap (2.76 eV) and relatively positive conduction band minimum (+0.38 eV), which lies above the CO_2/CO (−0.53 eV vs. NHE) and CO_2/CH_4 (−0.24 eV vs. NHE) redox potentials, rendering photogenerated electrons thermodynamically incapable of efficiently reducing CO_2 [40]. Additionally, the fast electron–hole recombination within WO_3, as evidenced by PL analysis and moderate surface area (24.1 $m^2\ g^{-1}$), further limits its photocatalytic efficiency. For $MgIn_2S_4$, the CH_4 and CO production rates increased to 3.41 μmol $g^{-1}\ h^{-1}$ and 4.48 μmol $g^{-1}\ h^{-1}$, respectively. The improvement is attributed to its narrower bandgap (2.13 eV) and more negative conduction band potential (−0.65 eV), which provides sufficient reduction power to activate CO_2 molecules. However, its limited light-harvesting surface and relatively low charge-separation efficiency restrict its overall performance [41].

The $MgIn_2S_4/WO_3$ heterostructures exhibited a substantial enhancement in CO_2 conversion activity due to the formation of a *Z*-scheme charge-transfer pathway that effectively separates photogenerated carriers and preserves strong redox potentials. The CH_4 and CO yields for the 5 wt% $MgIn_2S_4/WO_3$ composite reached 8.13 μmol $g^{-1}\ h^{-1}$ and 7.53 μmol $g^{-1}\ h^{-1}$, respectively, while the 15 wt% composite further improved these values to 19.7 μmol $g^{-1}\ h^{-1}$ (CH_4) and 10.72 μmol $g^{-1}\ h^{-1}$ (CO). The catalytic activity peaked for the 25 wt% $MgIn_2S_4/WO_3$ sample, which achieved 35.27 μmol $g^{-1}\ h^{-1}$ of CH_4 and 18.01 μmol $g^{-1}\ h^{-1}$ of CO, representing approximately 10-fold and 12-fold enhancements compared to pristine WO_3 [42]. This remarkable performance originates from several synergistic factors: (i) optimized interfacial contact between $MgIn_2S_4$ nanosheets and WO_3 nanoparticles, confirmed by SEM and TEM analyses, which facilitates rapid charge migration; (ii) enlarged specific surface area (71.9 $m^2\ g^{-1}$) and higher pore volume, offering abundant CO_2 adsorption sites; (iii) oxygen vacancies revealed by XPS O 1 s spectra, acting as electron traps and CO_2 activation centers; and (iv) preserved crystallinity and well-aligned band edges verified by XRD and optical analyses [43].

When the WO_3 loading increased further to 35 wt%, the CH_4 and CO yields slightly decreased to 27.62 μmol $g^{-1}\ h^{-1}$ and 13.29 μmol $g^{-1}\ h^{-1}$, respectively, mainly due to partial surface shielding of $MgIn_2S_4$ active sites and reduced light absorption efficiency. This trend confirms that excessive WO_3 coverage disrupts the interfacial balance essential for efficient *Z*-scheme operation. The reproducibility and long-term stability of the optimized 25 wt% $MgIn_2S_4/WO_3$ catalyst were examined through successive recycling runs (**Fig. 3c**). The CH_4 and CO yields remained nearly constant (≈105.8 μmol $g^{-1}\ h^{-1}$ and 55.8 μmol $g^{-1}\ h^{-1}$, respectively, over multiple 12 h cycles), indicating excellent structural stability and resistance to photocorrosion [44]. The linear product accumulation with irradiation time further confirms the sustained charge-transfer efficiency and the absence of catalyst deactivation. Mechanistically, under visible-light excitation, both $MgIn_2S_4$ and WO_3 are photoactivated [45]. Electrons in the conduction band of WO_3 (+0.38 eV) readily recombine with holes in the valence band of $MgIn_2S_4$ (+1.48 eV), forming a direct Z-scheme system. This process preserves highly reductive electrons in the $MgIn_2S_4$ conduction band (−0.65 eV) and strong oxidative holes in the WO_3 valence band (+3.14 eV). The former efficiently reduces CO_2 to CO and CH_4 via successive proton-coupled electron transfer steps, while the latter drives water oxidation to generate O_2 and protons, maintaining overall charge neutrality.

3.3. Optimizing the TC photodegradation condition over optimized 25%-$MgIn_2S_4/WO_3$ catalyst by RSM-CCD strategy

3.3.1. Model adequacy and accuracy

To statistically optimize the operating conditions governing TC degradation over the optimized 25 wt% $MgIn_2S_4/WO_3$ catalyst, a response surface methodology based on central composite design (RSM-CCD) was employed. Four major parameters—initial TC concentration (A), catalyst dosage (B), irradiation time (C), and solution pH (D)—were examined within the selected experimental domain to establish a predictive quadratic model correlating these factors with TC removal efficiency. The model adequacy and accuracy were first evaluated through diagnostic plots and ANOVA statistics. As shown in Fig. 3d, the close alignment of the data points along the 45° line in the predicted vs. actual plot confirms an excellent correlation between the experimental and model-predicted values. This strong linearity reflects the model's capability to reliably capture the experimental variability and accurately describe the relationship between the studied factors and TC degradation [46]. The Cook's distance plot (Fig. 3e) demonstrates that all data points fall well below the threshold of 1.0, indicating the absence of influential outliers or leverage points that could distort regression accuracy. This validates the uniform distribution of experimental runs and ensures statistical consistency across the design matrix. Furthermore, the normal probability plot of externally studentized residuals (Fig. 3f) exhibits a nearly straight-line pattern, revealing that the residuals follow a normal distribution with no systematic deviation. Collectively, these diagnostic plots substantiate that the quadratic model satisfies the assumptions of normality, homoscedasticity, and independence, confirming its suitability for predictive optimization.

The ANOVA results summarized in Table S2 reinforce the statistical significance of the quadratic model. The very high F-value (521.87) and an extremely low *p*-value (< 0.0001) indicate that the regression is highly significant, with less than a 0.01% probability of such a large F-value arising by random noise [47,48]. Among the individual terms, all

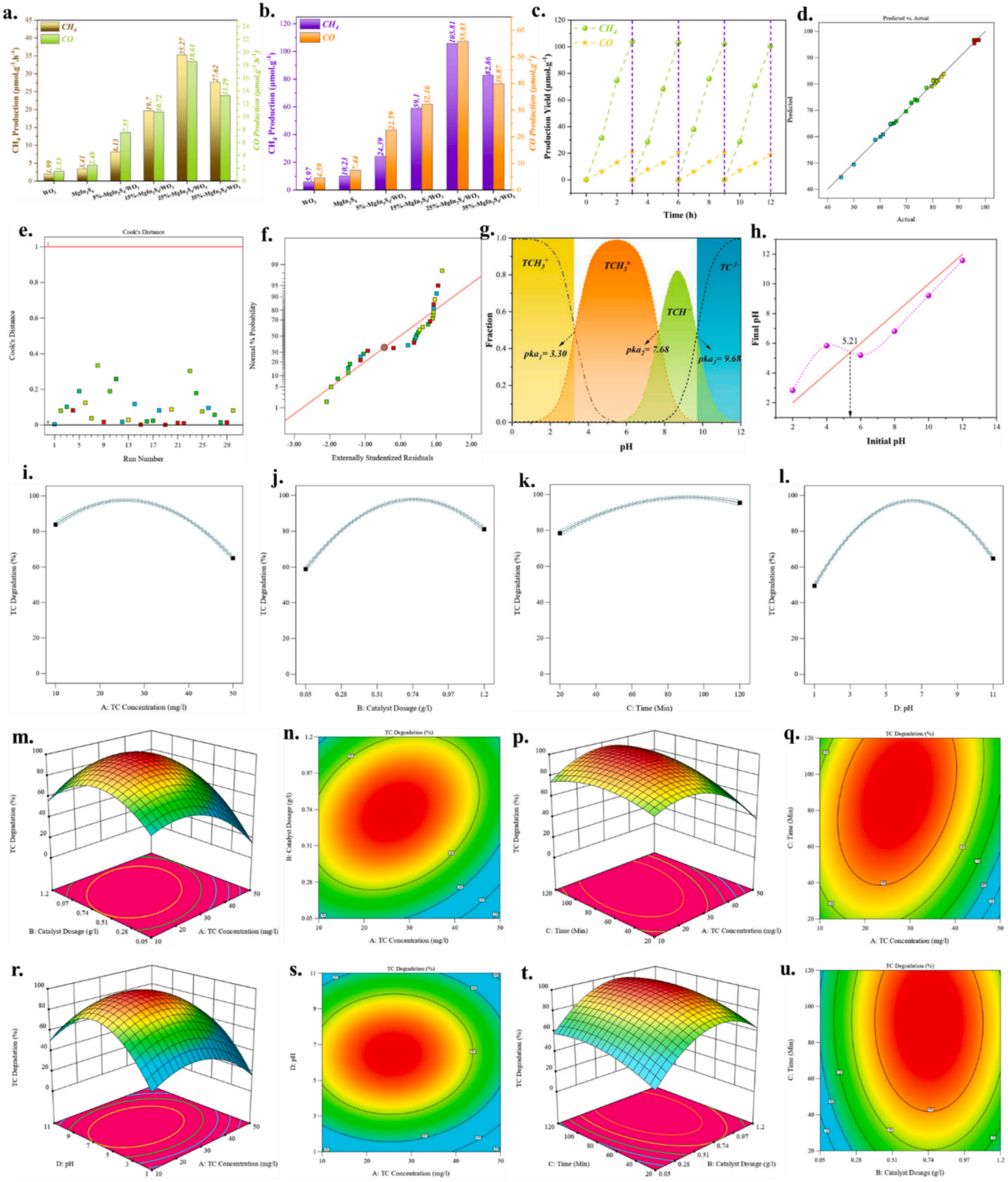

Fig. 3. (a–c) CO_2 reduction to CH_4 and CO under varying catalyst compositions and times; (d–f) model adequacy plots (Cook's distance, residual normality, predicted vs. actual); (g–h) TC speciation and pH_pzc (5.21) of 25 wt% $MgIn_2S_4/WO_3$; (i–l) effects of TC concentration, catalyst dosage, time, and pH on TC degradation; (m–u) 3D and contour plots showing parameter interactions, confirming optimal conditions at 26.95 mg L^{-1} TC, 0.69 g L^{-1} catalyst, 64.5 min, and pH 6.62 with 97.7% TC degradation.

main effects (A, B, C, D), several two-factor interactions (AB, AC, BD, CD), and the quadratic terms (A^2, B^2, C^2, D^2) were significant contributors ($p < 0.05$), while interactions AD and BC were statistically insignificant ($p > 0.10$). The insignificant lack-of-fit ($F = 1.67$, $p = 0.2972$) relative to pure error further demonstrates that the model fits the experimental data adequately, without systematic bias [49].

The fit-statistical parameters (Table S3) confirm the robustness and predictive strength of the model. The coefficient of determination ($R^2 = 0.9980$) and the adjusted R^2 (0.9960) indicate that more than 99% of the variability in TC degradation can be explained by the model, leaving less than 1% attributed to random error. Moreover, the predicted R^2 (0.9902) is in close agreement with the adjusted R^2, with a difference of only 0.0058, well below the acceptable threshold of 0.2, validating the model's strong predictive reliability. The low standard deviation (0.9203) and coefficient of variation (1.20%) highlight excellent model precision and repeatability, while the adequate precision ratio of 80.01 — far exceeding the minimum criterion of 4 — confirms a high signal-to-noise ratio, ensuring adequate discrimination of the experimental response [50]. Overall, these statistical and diagnostic results unequivocally confirm that the developed quadratic RSM-CCD model is highly reliable and predictive for describing the photocatalytic degradation of TC over the 25 wt% $MgIn_2S_4/WO_3$ heterostructure.

3.3.2. pH-oriented behavior and optimization of condition

The solution pH profoundly influences both the chemical speciation of TC and the surface charge characteristics of the 25%-$MgIn_2S_4/WO_3$ photocatalyst, thereby dictating adsorption affinity and overall photodegradation performance. As shown in Fig. 3 g, TC exists in multiple protonation states depending on the pH, defined by its dissociation constants of $pK_{a1} = 3.30$, $pK_{a2} = 7.68$, and $pK_{a3} = 9.68$. At pH < 3.3, TC exists mainly as the cationic TCH_3^+, while in the intermediate range (3.3 < pH < 7.7), it predominantly occurs as the zwitterionic form TCH_2^0, possessing both positive and negative functional moieties. At higher pH (> 9.7), TC transforms into mono- and di-anionic species (TCH^- and TC^{2-}), which exhibit electrostatic repulsion toward negatively charged photocatalyst surfaces [51]. The correlation between initial and final pH values during photodegradation, shown in Fig. 3 h, reveals a near-equilibrium region at pH = 5.21, indicating the point at which proton exchange between TC and the photocatalyst surface reaches steady-state. This behavior suggests that at slightly acidic to near-neutral conditions, the charge distribution of the 25%-$MgIn_2S_4/WO_3$ heterostructure and the zwitterionic TC species are favorably aligned. The WO_3 component ($pH_{PZC} \approx 6.2$) tends to exhibit mild positive surface charge under these conditions, while $MgIn_2S_4$, owing to surface S^{2-} sites, contributes localized negative potential regions. This dual charge environment enhances interfacial adsorption through electrostatic attraction, hydrogen bonding, and π–π stacking interactions with TC aromatic rings, facilitating subsequent oxidative and reductive reactions. At excessively low pH, competition from H^+ ions suppresses TC adsorption by protonating both catalyst and pollutant surfaces, whereas at high pH (> 9), the generation of negatively charged TC^{2-} species and excessive OH^- ions weakens electrostatic attraction and scavenges photoinduced holes, reducing the production of •OH radicals. Consequently, the photocatalytic efficiency decreases in strongly acidic or alkaline environments, emphasizing that the slightly acidic to near-neutral region provides the most favorable condition for TC degradation [52].

The response optimizer analysis (Fig. S1) quantitatively validated these mechanistic observations by predicting the optimal operational parameters for maximum TC degradation. The RSM-CCD optimization model identified the following ideal conditions: TC concentration = 26.95 mg L^{-1}, catalyst dosage = 0.69 g L^{-1}, irradiation time = 64.50 min, and pH = 6.62, achieving a predicted degradation efficiency of 97.69% with a desirability index of 1.000. These conditions correspond closely with the speciation regime where TC exists primarily in its zwitterionic form (TCH_2^0) and the photocatalyst surface carries balanced charge states, thus maximizing adsorption–reaction synergy. Hence, the integrated physicochemical interpretation of Figs. 3 g–3 h and Fig. 4e establishes that the optimal TC degradation occurs at near-neutral pH ≈ 6.6, where molecular interactions between TC and the $MgIn_2S_4/WO_3$ interface are maximized, ensuring efficient photon utilization, interfacial charge transfer, and radical-mediated oxidation. These optimized parameters were subsequently employed for kinetic modeling and mechanistic studies discussed in the following sections.

3.3.3. Effect of operational parameters

To elucidate the influence of individual process variables on photocatalytic performance, a series of 30 experiments were conducted according to the RSM-CCD design (**Table S4**), varying the initial TC concentration (10–50 mg L^1), catalyst dosage (0.05–1.2 g L^1), irradiation time (20–120 min), and pH (111). The corresponding degradation efficiencies ranged from 45.19% to 97.69%, confirming that all four factors substantially influence the systems photocatalytic response. The single-factor trends derived from the model predictions are illustrated in Figs. 3L–3 l. The initial concentration of TC significantly impacts the photocatalytic degradation rate by altering both the surface coverage on the catalyst and the optical density of the suspension. As evident from the data (runs 1, 3, 4, 10, 13, 17, 20, 23, and 26) and Fig. 3i, the degradation efficiency initially increases with TC concentration, reaching an optimum of 97.7% at 26.95 mg L^1, beyond which it gradually declines. At low TC concentrations (< 20 mg L^1), the limited availability of TC molecules results in inefficient utilization of photogenerated charge carriers, leading to moderate degradation efficiencies (e.g., 58.14–79.63%). As the concentration increases to ~27 mg L^1, more molecules occupy surface-active sites, enhancing charge transfer and radical attack processes, thus promoting higher removal. However, when the concentration exceeds 40 mg L^1, the degradation efficiency drops markedly (to 60–65%) due to two competing effects: (i) light attenuation within the solution (inner filter effect), which limits photon absorption by the catalyst, and (ii) competitive adsorption among excess TC molecules, resulting in site saturation and accumulation of partially oxidized intermediates that hinder active-site regeneration [53]. This bell-shaped behavior highlights the importance of balancing pollutant loading and photon accessibility for efficient photocatalysis.

The effect of catalyst dosage on TC degradation is shown in **Fig. 3j** and corroborated by experimental runs 5, 7, 11, 12, 16, 18, 24, 26, and 29. The degradation efficiency increases sharply with increasing catalyst loading up to 0.69 g L^1, achieving a maximum of 97.7%, and then gradually decreases when the dosage exceeds 0.9 g L^1. At lower dosages (0.05–0.3 g L^1), the number of active sites and absorbed photons is insufficient, leading to incomplete oxidation (58–70%). Increasing the dosage enhances photon absorption, charge carrier generation, and availability of reactive oxygen species ($•O_2$ and •OH), thereby improving degradation efficiency. However, beyond the optimal loading, the suspension becomes optically dense, causing light scattering and reduced effective illumination of interior catalyst particles. Excess catalyst may also promote particle agglomeration and recombination of photogenerated carriers, diminishing quantum efficiency [54,55]. Thus, 0.69 g L^{-1} is identified as the optimal dosage, providing a balance between photon harvesting and surface availability.

The influence of irradiation time was investigated between 20 and 120 min (runs 4, 6, 10, 14, 17, 19, 20, 26). As shown in Fig. 3 k, the TC degradation efficiency increases progressively with exposure time, approaching saturation after approximately 65 min, which corresponds to the predicted optimum of 97.69%. During the initial stages (0–40 min), rapid degradation occurs due to the abundance of active radicals and accessible TC molecules on the surface. With prolonged illumination, most TC molecules are oxidized, and the system reaches quasi-equilibrium as intermediate species compete for adsorption. Extending the reaction beyond 90 min yields negligible improvement, indicating that nearly all accessible pollutants have been mineralized. These findings confirm that 65 min is sufficient to reach steady-state photocatalytic activity under visible-light conditions, beyond which energy input offers

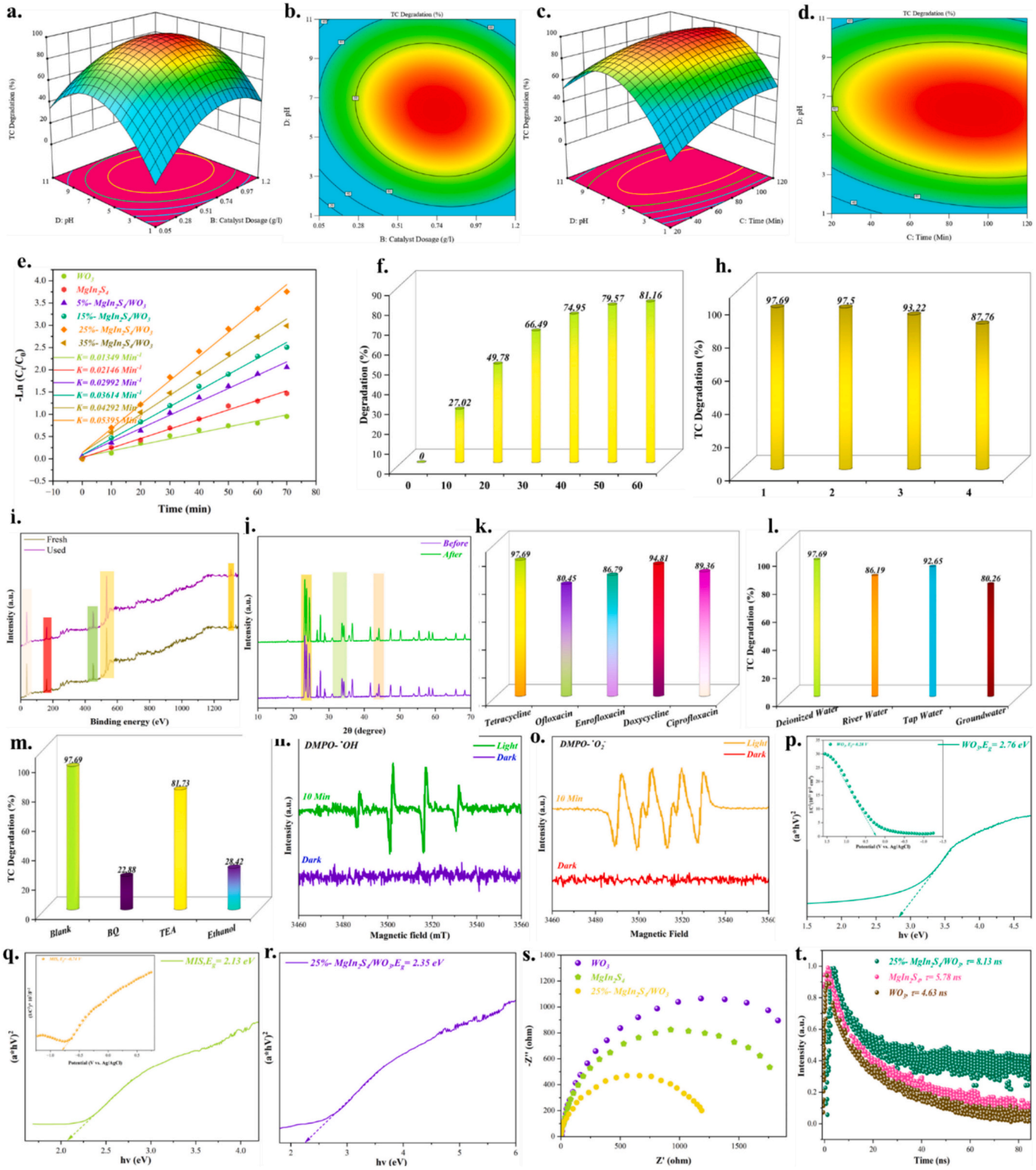

Fig. 4. (a–d) Response surface plots showing the effects of pH, dosage, and time on TC degradation; (e–f) kinetic and TOC analyses; (g) recyclability over four cycles; (h–i) XPS and XRD stability; (j–k) degradation of various antibiotics and performance in different water sources; (l–m) radical-trapping and ESR spectra confirming •OH and $•O_2^-$ generation; (n–p) Tauc plots of $MgFe_2S_4$, Bi_2WO_6, and 25% $MgFe_2S_4/Bi_2WO_6$; (q–r) EIS and PL results demonstrating enhanced charge transfer and longer carrier lifetime in the optimized heterostructure.

minimal gains in efficiency [56].

Solution pH exerts a multifaceted effect on TC degradation, influencing both the surface charge of the $MgIn_2S_4/WO_3$ heterostructure and the ionization state of TC molecules. The degradation profile (Fig. 3 l) exhibits a clear parabolic trend: efficiency increases from strongly acidic conditions to an optimum near pH = 6.6, followed by a decline at higher pH levels. At low pH (< 3.5), protonation of both catalyst and TC molecules results in electrostatic repulsion between positively charged

species, reducing adsorption affinity and radical attack probability (45–60%). Near-neutral conditions favor the zwitterionic TC form (TCH_2^0) and balanced surface charges on $MgIn_2S_4$ (slightly negative) and WO_3 (slightly positive), enabling strong electrostatic and hydrogen-bond interactions. This synergistic state maximizes interfacial charge transfer and reactive radical formation, leading to the highest removal efficiency (~97.7%). Under alkaline conditions (> 9), TC transforms into anionic species (TCH/TC^2), while the catalyst surface becomes increasingly negative, inducing repulsive interactions and reducing •OH radical formation due to competitive scavenging by OH ions [57].

3.3.4. Analysis of interactive effects and 3D response-surface optimization

The three-dimensional (3D) response surfaces and their corresponding contour maps (Figs. 3 m–3u) provide a visual interpretation of how pairs of operational parameters interact to govern TC degradation over the optimized 25 wt% $MgIn_2S_4/WO_3$ photocatalyst. All surfaces exhibit pronounced curvature and well-defined maxima, confirming that the degradation response follows a quadratic relationship rather than simple linear dependence—consistent with the significant interaction and square terms in **Table S2**. A distinct elliptical dome is observed, with the highest response located near A = 27 mg L^1 and B = 0.7 g L^1 (Figs. 3 m–3n). The ellipticity of the contour lines implies a strong coupling between pollutant loading and catalyst density, where excessive values of either factor shift the system away from the optimum. This curvature reflects the balance between photon absorption and surface availability: once the particle density exceeds the photon penetration limit, the additional active sites contribute little to overall degradation [58]. The smooth gradient of the contour field also indicates that small deviations around the optimum cause a measurable efficiency loss, underscoring the process sensitivity predicted by the large AB F-value (175.60).

The 3D topology reveals a moderately steep ridge rather than a broad plateau, suggesting that time acts as an amplifying factor only within the appropriate concentration window (Figs. 3o–3p). At low pollutant loading, prolonged exposure rapidly saturates the available active sites; at higher concentrations, the slope flattens, revealing diminished photon accessibility. The transition of color intensity along the diagonal of the contour plot illustrates this synergistic limitation, where both parameters must co-evolve to maintain near-maximum degradation. Such a ridge-type surface typically signifies that the kinetic regime shifts from photon-limited to adsorption-limited as A increases—a behavior consistent with heterogeneous photocatalytic dynamics. A symmetric elliptical surface centered around pH= 6–7 demonstrates that pH moderates the concentration effect through surface-charge regulation (Figs. 3q–3r). The well-defined circular contour indicates that moderate shifts in pH away from neutrality rapidly suppress the degradation rate even at optimal concentration, confirming that both variables jointly define the charge-transfer environment at the solid–liquid interface. The compact high-response region (deep red zone) evidences a narrow operational window where electrostatic attraction and radical generation are simultaneously maximized, validating the strong AD interaction derived from the model statistics.

The nearly circular contour of this pair denotes a mild but cooperative interaction, meaning that either longer exposure or higher catalyst loading alone can compensate partially for the other within moderate limits (Figs. 3 t–3u). However, the dome's apex remains confined near B = 0.7 g L^1 and C = 65 min, beyond which the response decays smoothly. The gentle curvature reflects an energy-efficiency threshold: additional light input or catalyst mass yields diminishing marginal improvement because radical generation already approaches steady-state. This pattern aligns with the small curvature of the BC surface term, suggesting that while time and dosage are individually influential, their joint contribution is primarily additive. Maximum degradation (~97.7%) occurs near pH = 6.5 and dosage = 0.7 g L^1. At low dosage, pH changes have little effect due to limited active sites, while at higher loading, efficiency becomes highly pH-dependent (Figs. 4a–4b). The decline under acidic and alkaline conditions arises from electrostatic repulsion between charged TC species and catalyst surfaces. Near-neutral pH favors zwitterionic TC adsorption and balanced surface potential, enhancing interfacial charge transfer. The pronounced curvature agrees with the significant BD interaction ($F = 66.51$, $p < 0.0001$) [59]. Degradation improves with longer irradiation, but only around pH 6–7, where radical formation and charge-carrier separation are optimized (Figs. 4c–4d). The ridge-like plateau in this region indicates cooperative control of oxidation kinetics by both pH and exposure time. Deviation toward strong acidity or alkalinity suppresses efficiency due to protonation/deprotonation effects on surface redox sites.

3.4. Kinetic study, reusability, stability and adaptivity

To elucidate the reaction kinetics governing TC degradation over the synthesized photocatalysts, the experimental data were fitted to a pseudo-first-order kinetic model, expressed as: $\ln(C_0/C_t) = kt$ where C0 and Ct denote the initial and instantaneous concentrations of TC, respectively, and k represents the apparent rate constant (min^1). The kinetic profiles and their corresponding rate constants are shown in Fig. 4e. The linearity of the plots with high correlation coefficients ($R^2 >$ 0.98 for all samples) confirms that the degradation of TC follows pseudo-first-order kinetics, implying that the rate is primarily governed by the surface availability of reactive sites and photon-induced charge carrier dynamics. The apparent rate constants were calculated as 0.01349, 0.02146, 0.02992, 0.03614, 0.04292, and 0.05395 min^{-1} for WO_3, $MgIn_2S_4$, 5%-$MgIn_2S_4/WO_3$, 15%-$MgIn_2S_4/WO_3$, 25%-$MgIn_2S_4/WO_3$, and 35%-$MgIn_2S_4/WO_3$, respectively. A progressive enhancement in reaction rate with increasing $MgIn_2S_4$ loading confirms the beneficial role of heterojunction coupling between the n-type WO_3 and p-type $MgIn_2S_4$. Among all composites, the 25 wt% $MgIn_2S_4/WO_3$ catalyst exhibited the highest rate constant (k = 0.05395 min^1), approximately fourfold higher than pristine WO_3 and 2.5 times greater than pure $MgIn_2S_4$. This superior kinetic performance arises from the optimal interfacial contact between the two semiconductors, which promotes efficient charge separation and transfer via a *Z*-scheme mechanism. Under illumination, photoexcited electrons from the conduction band (CB) of $MgIn_2S_4$ (−0.65 eV) recombine with holes from the valence band (VB) of WO_3 (+3.14 eV), preserving the strong redox potentials of the remaining electrons in WO_3's CB (+0.38 eV) and holes in $MgIn_2S_4$'s VB (+1.48 eV). This configuration facilitates simultaneous generation of $•O_2$ and •OH radicals, both crucial for oxidative degradation of TC molecules [60]. However, when the $MgIn_2S_4$ content exceeded 25 wt% (i.e., 35 wt%), the rate constant slightly decreased to 0.04292 min^{-1}, likely due to partial light shielding and active-site coverage caused by excessive $MgIn_2S_4$ aggregation. Such overloading can obstruct photon penetration and reduce interfacial charge mobility. Therefore, the 25 wt% composite is identified as the optimum configuration, balancing light absorption, surface activity, and charge transport.

The long-term performance of the optimized 25 wt% $MgIn_2S_4/WO_3$ photocatalyst was evaluated through TOC mineralization, cyclic reusability, and structural stability analyses (Figs. 4f–4j). Under the optimal RSM-CCD conditions (TC = 26.95 mg L^{-1}, catalyst dosage = 0.69 g L^1, irradiation time = 64.5 min, and pH = 6.62), the photocatalyst achieved a TC degradation efficiency of 97.69%, corresponding to a TOC removal of 81.16% (**Fig. 4f**). The high TOC conversion confirms not only the effective breakdown of tetracycline molecules but also extensive mineralization into CO_2 and H_2O. The gradual increase in TOC removal with irradiation time—rising from 27.02% at 10 min to 81.16% at 60 min—demonstrates sustained generation of oxidative radicals ($•O_2^-$ and •OH) and efficient photocarrier utilization throughout the reaction. The photocatalyst exhibited outstanding cyclic durability (**Fig. 4 g**). Even after four successive runs, the degradation efficiency only slightly decreased from 97.69% to 87.76%, indicating minimal catalyst deactivation. The small loss can be attributed to partial surface coverage by organic intermediates and minor catalyst loss during washing and

recovery steps. Post-reaction XPS and XRD analyses (Figs. 4 **h–4j**) further confirmed the structural stability of the heterojunction. The XPS spectra of the used sample retained the original core-level peaks of W 4f, In 3d, S 2p, Mg 1 s, and O 1 s without notable energy shifts, suggesting that the chemical composition and oxidation states were preserved. Similarly, the XRD diffractograms of fresh and used catalysts displayed identical diffraction peaks corresponding to monoclinic WO_3 and spinel $MgIn_2S_4$, indicating no structural collapse or phase transformation after multiple cycles.

The photocatalyst demonstrated remarkable universality in degrading structurally distinct fluoroquinolone and tetracycline antibiotics (Fig. 4 **k**). The degradation efficiencies followed the order: Tetracycline (97.69%) > Doxycycline (94.81%) > Ciprofloxacin (89.36%) > Enrofloxacin (86.79%) > Ofloxacin (80.45%). The slightly lower efficiencies for fluoroquinolones (CIP, ENR, OFL) are attributed to their more stable aromatic rings and electron-withdrawing substituents (—F, –COOH), which hinder radical attack compared with the more electron-rich phenolic and amide sites in tetracyclines. Meanwhile, the structural similarity between TC and doxycycline, both containing conjugated carbonyl–amino systems, facilitates π–π interactions with the WO_3 surface and accelerates charge-transfer oxidation through the S-scheme heterojunction [61]. These results affirm that the $MgIn_2S_4/WO_3$ catalyst possesses broad-spectrum photocatalytic activity, efficiently decomposing diverse antibiotic pollutants under visible light.

To verify the catalysts environmental robustness, TC degradation was evaluated in representative real-water matrices, including deionized (DI) water, tap water, river water, and groundwater (Fig. 4 l). The corresponding removal efficiencies were 97.69%, 92.65%, 86.19%, and 80.26%, respectively. The gradual decline in activity from DI water to natural waters can be reasonably attributed to matrix effects arising from dissolved inorganic ions (e.g., Cl, HCO_3, SO_4^{2}) and dissolved organic matter (DOM), which influence heterogeneous photocatalysis through multiple coupled mechanisms. Inorganic ions may compete with TC for adsorption sites and can also scavenge reactive oxidants or redirect radical chemistry; for example, HCO_3/CO_3^{2} and Cl can consume $^{\bullet}OH$ or convert it into less reactive radicals (e.g., $^{\bullet}CO_3$), thereby lowering the effective oxidative capacity and altering pathway distribution. In parallel, DOM—commonly represented by humic acid (HA) can attenuate incident light via the inner-filter (light-shielding) effect, decreasing photon utilization and suppressing charge generation; it can additionally quench reactive species (particularly •OH and, in some cases, photogenerated holes), reducing the steady-state concentration of active oxidants available for TC conversion. Moreover, HA/DOM may adsorb on the catalyst surface, leading to partial site blocking (surface fouling) and competitive adsorption against TC, which further decreases interfacial reaction probability even when reactive oxygen species are present [62–64]. Collectively, these well-known matrix effects rationalize the observed inhibition trend (DI > tap > river > groundwater). Despite these realistic interferences, the catalyst maintained more than 80% TC removal across all tested waters, indicating strong adaptability and sufficiently high redox capability under ion-/DOM-containing conditions. The relatively limited performance decay in complex matrices further suggests that the $MgIn_2S_4/WO_3$ interface sustains efficient charge separation and oxidative functionality, supporting its potential for practical water-treatment applications.

3.5. Reactive species and optical properties

To identify the dominant reactive oxygen species (ROS) responsible for the photocatalytic degradation of TC by the optimized 25 wt% $MgIn_2S_4/WO_3$ heterojunction, a series of radical trapping and electron spin resonance (ESR) experiments were performed, as presented in Figs. 4 **m–4o**. The reactive species quenching experiments were conducted using benzoquinone (BQ), triethanolamine (TEA), and ethanol as scavengers for superoxide radicals ($\bullet O_2$), photogenerated holes (h^+), and hydroxyl radicals (•OH), respectively. In the absence of any scavenger (blank), the degradation efficiency of TC reached 97.69%, indicating the catalyst's strong intrinsic photoactivity (Fig. 4 **m**). Upon the addition of BQ, the efficiency sharply decreased to 22.88%, demonstrating that $\bullet O_2$ radicals play the most critical role in the photodegradation process. When TEA was introduced, the degradation efficiency moderately declined to 81.73%, confirming that h^+ also contributes significantly, likely through direct oxidation of TC and generation of •OH radicals via water oxidation. Conversely, the presence of ethanol resulted in a notable drop to 28.42%, suggesting that •OH radicals are the secondary but still essential oxidizing species. These findings collectively reveal that the degradation of TC over $MgIn_2S_4/WO_3$ primarily follows an oxidative pathway dominated by $\bullet O_2$ and •OH radicals, with photogenerated holes acting synergistically to sustain radical generation and prevent recombination.

To further validate the formation of reactive radicals, ESR spectra were recorded using DMPO (5,5-dimethyl-1-pyrroline N-oxide) as a spin-trapping agent (Fig. 4**n**). As shown in Fig. 4n, no ESR signal was observed in the dark, while upon visible-light irradiation, four characteristic peaks appeared corresponding to the DMPO–•OH adduct, confirming the generation of hydroxyl radicals. The sharp intensity of these peaks after 10 min of irradiation indicates the high oxidative ability of the catalyst and the efficient charge separation that facilitates surface reactions involving water or surface –OH groups. Similarly, Fig. 4**o** shows the ESR spectra for DMPO–$\bullet O_2$ under dark and light conditions. Distinct four-line signals were detected under light irradiation, while no signal appeared in the dark, verifying the light-induced formation of superoxide radicals [65]. The presence of $\bullet O_2^-$ radicals suggests that photogenerated electrons from the conduction band (CB) of WO_3 or $MgIn_2S_4$ effectively react with dissolved oxygen molecules, forming reactive intermediates responsible for oxidative degradation of TC.

To elucidate the electronic structure and interfacial charge transfer characteristics of the photocatalysts, UV–vis DRS and Mott–Schottky (M–S) analyses were performed, as shown in Figs. 4p–4r. These analyses provide insights into the band gap energy (E_g), flat-band potential (E_{fb}), and consequently, the positions of the conduction band (CB) and valence band (VB) edges, which are essential for understanding the charge-transfer mechanism in the $MgIn_2S_4/WO_3$ heterojunction. The optical absorption spectra, plotted as $(\alpha h\nu)^2$ versus $h\nu$, were used to determine the band gap energies by extrapolating the linear portions of the Tauc plots. The estimated band gaps were 2.76 eV for WO_3, 2.13 eV for $MgIn_2S_4$, and 2.35 eV for 25 wt% $MgIn_2S_4/WO_3$ composite. The pure WO_3 exhibits a relatively wide band gap, consistent with its intrinsic absorption limited to the near-UV and blue visible regions. In contrast, $MgIn_2S_4$, with a narrower band gap of 2.13 eV, efficiently harvests visible light up to ~580 nm. Upon coupling these two semiconductors, the composites band gap slightly widens to 2.35 eV compared to pristine $MgIn_2S_4$, indicating the formation of an interfacial potential gradient and partial electronic interaction at the heterojunction interface [66]. This moderate shift enhances visible-light absorption while maintaining sufficient redox potential, confirming the *Z*-scheme charge transfer pathway between $MgIn_2S_4$ and WO_3. The M–S plots, recorded at a frequency of 1 kHz, show positive slopes for both WO_3 and $MgIn_2S_4$, verifying their n-type semiconductor nature. The extrapolation of the linear region to the x-axis gives the flat-band potentials (E_{fb}), which approximate the CB edge for n-type materials. The E_{fb} values were obtained as +0.28 V (vs. Ag/AgCl) for WO_3 and 0.74 V (vs. Ag/AgCl) for $MgIn_2S_4$, corresponding to +0.38 V and 0.65 V vs. NHE, respectively, after potential conversion. Using the experimentally determined band gaps, the VB potentials were calculated as +3.14 V for WO_3 and + 1.48 V for $MgIn_2S_4$. These results imply that, in a conventional type-II configuration, photogenerated electrons in $MgIn_2S_4$ (CB: 0.65 eV) could transfer to WO_3 (CB: +0.38 eV), while holes migrate oppositely—however, such a transfer would lead to weakened redox potential. Therefore, considering the stronger oxidative and reductive capacities evidenced by ESR and scavenger tests, the electron–hole transfer is more consistent with a *Z*-scheme mechanism. In this configuration, photogenerated electrons

from the CB of WO_3 recombine with holes from the VB of $MgIn_2S_4$, leaving highly energetic electrons in $MgIn_2S_4$ (0.65 eV) and strongly oxidative holes in WO_3 (+3.14 eV). These charge carriers drive the formation of $\bullet O_2$ and •OH radicals, respectively, enabling the efficient degradation of tetracycline under visible-light irradiation.

The Nyquist plots show semicircles whose radii follow 25%–$MgIn_2S_4/WO_3$ < $MgIn_2S_4$ < WO_3 (Fig. 4 s). The composite exhibits the smallest arc (few hundred Ω range vs. 800–1100 Ω for $MgIn_2S_4$ and 900–1300 Ω for WO_3), indicating the lowest interfacial charge-transfer resistance (R_{ct}) at the electrode–electrolyte interface. In the usual Randles model, a smaller semicircle reflects faster interfacial electron transport and suppressed recombination. This agrees with the heterojunction creating an internal field and abundant mesoporosity (high BET area for the 25 wt% sample), both of which facilitate carrier migration to reactive sites [67].

TRPL decay curves fit well to a multi-exponential model, giving average lifetimes of WO_3: τ_{avg} = 4.63 ns, $MgIn_2S_4$: τ_{avg} = 5.78 ns, and 25%–$MgIn_2S_4/WO_3$: τ_{avg} = 8.13 ns (**Fig. 4 t**). The 40–75% lifetime extension in the composite verifies slower radiative recombination and more efficient carrier separation. This prolongation is consistent with a direct *Z*-scheme pathway: electrons in WO_3 (CB) recombine with holes in $MgIn_2S_4$ (VB), leaving strongly reducing electrons in $MgIn_2S_4$ (−0.65 eV) and highly oxidizing holes in WO_3 (+3.14 eV) available for surface reactions ($\bullet O_2^-$ and •OH formation shown earlier). Steady-state PL emission ($\lambda_{exc} \approx$ 360 nm) is highest for WO_3, lower for $MgIn_2S_4$, and lowest for 25%–$MgIn_2S_4/WO_3$ across 480–620 nm (**Fig. S2**). Reduced PL intensity denotes suppressed electron–hole recombination, corroborating TRPL and EIS results. The quenching arises from (i) intimate interfacial contact seen by SEM/TEM, (ii) band alignment that drives the Z-scheme charge flow, and (iii) defect/oxygen-vacancy states (XPS O 1 s) that act as shallow traps aiding charge separation rather than deep recombination centers.

3.6. Mechanistic insights of charge transfer pathways for photocatalytic processes

The mechanistic insight into the photocatalytic process of the 25 wt % $MgIn_2S_4/WO_3$ heterojunction is schematically illustrated in Fig. 5. Upon visible-light irradiation, both WO_3 and $MgIn_2S_4$ semiconductors are photoexcited, generating electron–hole (e^-/h^+) pairs according to the following reactions:

$$WO_3 + h\nu \rightarrow WO_3(e^-(CB) + h^+(VB)) \quad (1)$$

$$MgIn_2S_4 + h\nu \rightarrow MgIn_2S_4(e^-(CB) + h^+(VB)) \quad (2)$$

To elucidate the charge transfer pathway, two possible mechanisms—type-II and direct *Z*-scheme—must be compared. In a conventional type-II heterojunction, photogenerated electrons from the CB of $MgIn_2S_4$ (E_{CB} = 0.65 eV vs. NHE) migrate to the CB of WO_3 (E_{CB} = +0.38 eV), while the holes in the VB of WO_3 (E_{VB} = +3.14 eV) move to the VB of $MgIn_2S_4$ (E_{VB} = +1.48 eV). Although such migration spatially separates charge carriers, it simultaneously decreases the redox capability of both semiconductors [68].

Specifically, electrons accumulated in the WO_3 conduction band (+0.38 eV) possess insufficient reduction potential to convert CO_2 to CH_4 ($E(CO_2/CH_4)$ = 0.24 eV) or CO ($E(CO_2/CO)$ = 0.53 eV).Similarly, the transferred holes in the valence band of $MgIn_2S_4$ (+1.48 eV) lack the oxidation strength to generate hydroxyl radicals (•OH) from H_2O ($E(\bullet OH/H_2O)$ = +2.38 eV). Therefore, a type-II mechanism cannot drive simultaneous CO_2 reduction and pollutant degradation efficiently under visible light, as both redox half-reactions are thermodynamically unfavorable [69,70].

In contrast, the experimental observations—including enhanced charge lifetime (τ = 8.13 ns), reduced charge-transfer resistance, and intense ESR signals for $\bullet O_2$ and •OH radicals—support a direct *Z*-scheme mechanism. In this system, photogenerated electrons in the CB of WO_3 recombine with holes in the VB of $MgIn_2S_4$ at the heterointerface, as driven by the built-in internal electric field (IEF) and Fermi-level

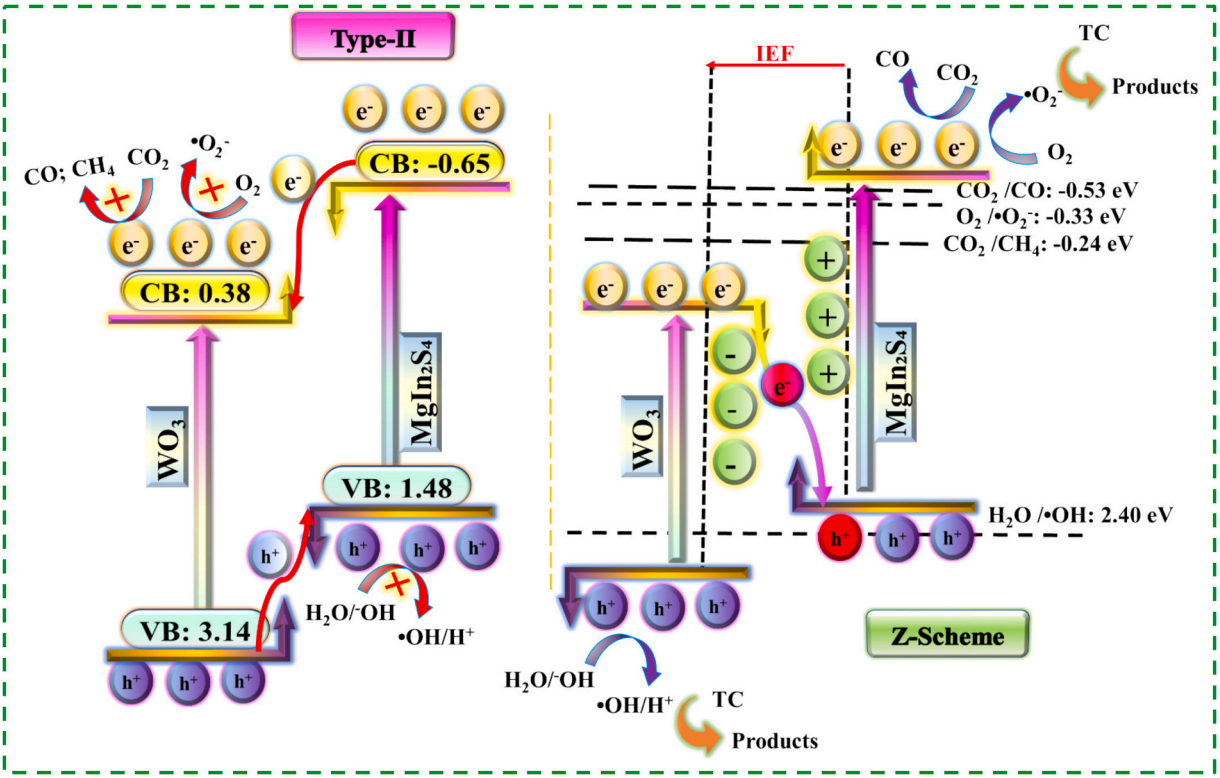

Fig. 5. Schematic of the charge transfer pathways for CO_2 conversion and TC degradation.

equilibration. This recombination leaves highly reductive electrons in the CB of $MgIn_2S_4$ (−0.65 eV) and highly oxidative holes in the VB of WO_3 (+3.14 eV), both possessing sufficient potential to initiate the surface redox reactions required for CO_2 conversion and pollutant degradation. The reactive electrons on the $MgIn_2S_4$ conduction band can reduce dissolved CO_2 via multi-electron transfer processes [71,72]:

$$CO_2 + e^- \rightarrow CO_2 \bullet^- \quad (3)$$

$$CO_2 \bullet^- + e^- + H^+ \rightarrow HCOO^- \quad (4)$$

$$HCOO^- + 6H^+ + 6e^- \rightarrow CH_3OH + H_2O \quad (5)$$

$$CO_2 + 8H^+ + 8e^- \rightarrow CH_4 + 2H_2O \quad (6)$$

$$CO_2 + 2H^+ + 2e^- \rightarrow CO + H_2O \quad (7)$$

Meanwhile, photogenerated holes in the VB of WO_3 oxidize surface-adsorbed H_2O or hydroxide ions to generate hydroxyl radicals (•OH), while electrons reduce O_2 molecules to superoxide radicals ($\bullet O_2^-$). These reactive oxygen species (ROS) synergistically degrade TC molecules via successive oxidation steps [73]:

$$h^+ + H_2O \rightarrow \bullet OH + H^+ \quad (8)$$

$$O_2 + e^- \rightarrow \bullet O_2^- \quad (9)$$

$$\bullet OH / \bullet O_2^- + TC \rightarrow CO_2 + H_2O + \text{intermediate species} \quad (10)$$

Such a *Z*-scheme arrangement ensures strong redox potentials for both oxidation and reduction half-reactions, unlike the compromised type-II structure. Furthermore, the spatial separation of active sites—oxidative WO_3 surface for •OH generation and reductive $MgIn_2S_4$ surface for CO_2 reduction—minimizes recombination losses. The internal electric field, as supported by Mott–Schottky results, accelerates directional charge migration, improving quantum efficiency and reaction kinetics. In conclusion, the 25 wt% $MgIn_2S_4/WO_3$ composite operates via a direct Z-scheme charge-transfer route rather than a type-II mechanism. This configuration maintains the high oxidative capacity of WO_3 and the strong reductive power of $MgIn_2S_4$, enabling effective dual-function photocatalysis for CO_2 reduction to CH_4/CO and complete mineralization of organic pollutants such as tetracycline. The superior photoinduced charge separation, supported by EIS, PL, TRPL, and ESR

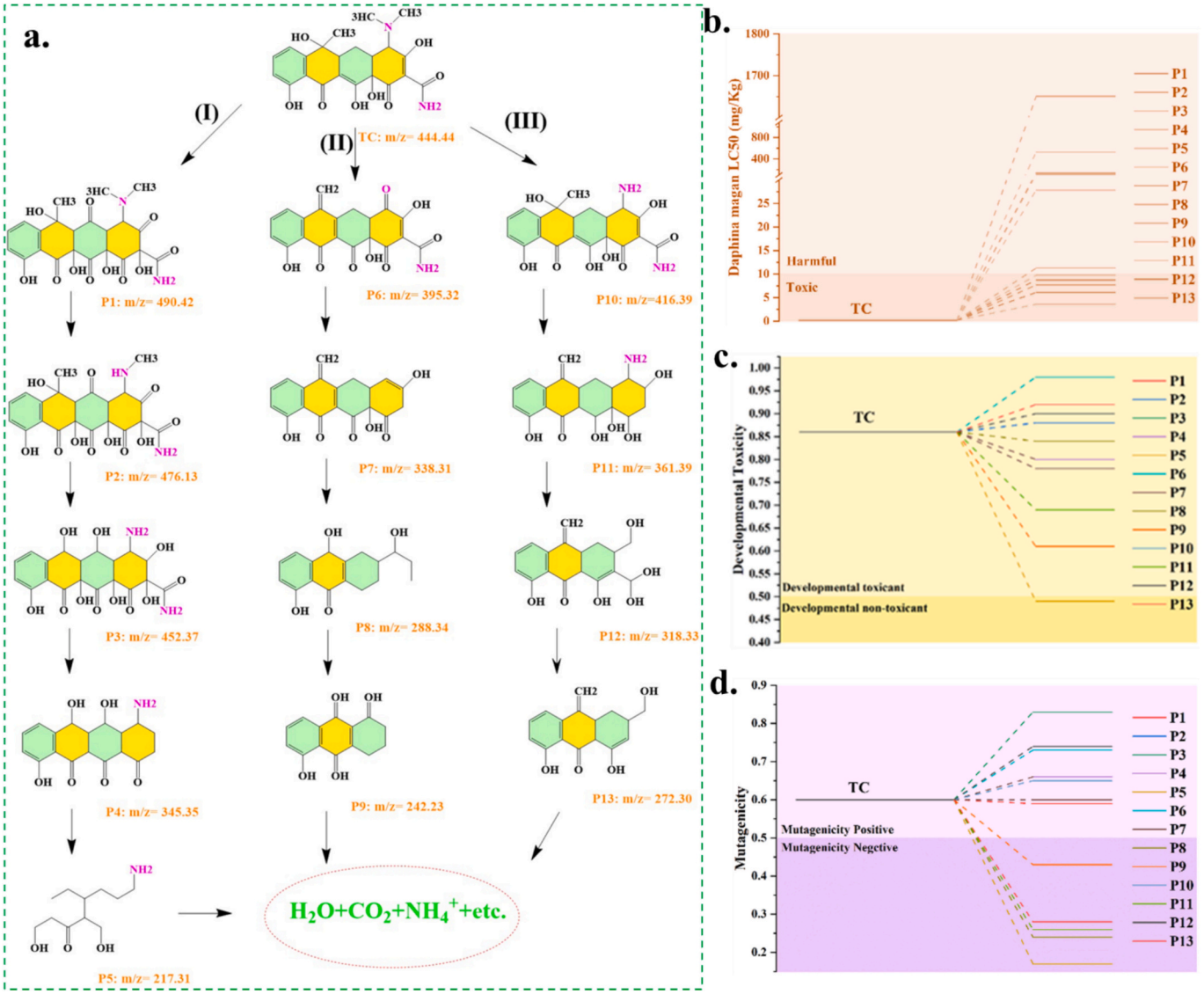

Fig. 6. (a) Proposed photocatalytic degradation pathways of TC over 25 wt% $MgIn_2S_4/WO_3$, showing sequential dealkylation, hydroxylation, and ring-opening reactions leading to mineralization into CO_2, H_2O, and NH_4^+. (b–d) Predicted acute toxicity, developmental toxicity, and mutagenicity of TC and intermediates (P1–P13), confirming markedly reduced toxicity and genotoxicity after photocatalytic degradation.

analyses, confirms the rationality of the Z-scheme model and itskey role in driving the observed photocatalytic enhancements.

3.7. Possible TC degradation pathways and toxicity assessment

To elucidate the transformation route of TC over the as-prepared photocatalyst under visible-light irradiation, the main degradation intermediates were identified by HPLC–MS and a multi-branch pathway network was proposed (Fig. 6a; **Fig. S3**). As shown in Fig. 6a, twelve major intermediates were detected with mass-to-charge (*m/z*). The progressive decrease in m/z values indicates that TC does not degrade through a single linear sequence; instead, several concurrent reactions proceed in parallel, including functional-group modification (e.g., dealkylation/demethylation, hydroxylation, and deamination), skeletal rearrangement, and ring-opening/fragmentation, ultimately leading to mineralization into small inorganic species (CO_2, H_2O, NH_4^+, etc.). Overall, the proposed degradation network involves three primary routes (I–III) governed by the synergistic oxidation of reactive oxygen species ($^{\bullet}O_2$ and $^{\bullet}OH$) together with photogenerated holes (h^+). Reactive-species trapping and ESR analyses demonstrate that TC conversion is mainly dominated by $^{\bullet}O_2$ and $^{\bullet}OH$, while h^+ contributes synergistically. Consistent with this evidence, Route I (P1 → P5) is proposed to be primarily driven by h^+/$^{\bullet}OH$-mediated oxidation, which favors early-stage oxidative transformations such as dealkylation/demethylation and hydroxylation. Specifically, the parent TC molecule (m/z = 444.44) undergoes oxidative dealkylation/demethylation of the dimethylamino group to yield P1 (m/z = 490.42), followed by stepwise hydroxylation and elimination of amino/hydroxyl functionalities to form P2–P4 through successive oxidation and structural opening [74]. Subsequently, the cleavage of C—N bonds and deamination reactions progressively simplify the molecular framework, producing smaller organic fragments (P5–P9). In contrast, Routes II (P6 → P9) and III (P10 → P13) are proposed to be $^{\bullet}O_2$-initiated transformation routes, in which superoxide-triggered reactions promote radical-assisted skeletal conversion and ring-opening/fragmentation, while subsequent $^{\bullet}OH$/h^+ oxidation accelerates deep degradation and mineralization. In parallel, keto–enol rearrangement and aromatic-ring hydroxylation can generate P10–P13, ultimately resulting in complete conversion into low-molecular-weight products such as H_2O, CO_2, and NH_4^+ [75]. The observed coexistence of pronounced $^{\bullet}OH$ and $^{\bullet}O_2^-$ activities is further consistent with a direct *Z*-scheme charge-transfer behavior in the 25 wt % $MgIn_2S_4/WO_3$ heterojunction. In this framework, the strongly oxidizing VB holes of WO_3 (+3.14 eV) can directly oxidize TC and/or generate $^{\bullet}OH$ from H_2O/–OH, while the highly reducing CB electrons of $MgIn_2S_4$ (0.65 eV) effectively activate dissolved O_2 to $\bullet O_2$[76]. This synergistic redox process accelerates the conversion of TC into non-aromatic fragments and, eventually, inorganic species, highlighting the multi-step oxidation, deamination, and ring-opening reactions responsible for the overall mineralization outcome.

In evaluating the environmental applicability of the 25 wt% $MgIn_2S_4/WO_3$ photocatalyst, the toxicity of TC and its degradation intermediates was further assessed using the Toxicity Estimation Software Tool (TEST). As depicted in Figs. 6b–6d, the acute toxicity (LC_{50}) toward *Daphnia magna*, developmental toxicity, and mutagenicity were analyzed. The LC_{50} value of the parent TC was approximately 0.1 mg/kg, indicating significant toxicity. In contrast, most intermediates exhibited much higher LC_{50} values (>200 mg/kg), reflecting their lower aquatic toxicity. Fig. 6c shows that although several intermediates remain developmentally toxic (e.g., P1–P4), the majority exhibit reduced developmental toxicity relative to the parent compound. Similarly, as shown in Fig. 6d, the mutagenicity of TC (initial value 0.6) decreases considerably for most by-products, transitioning from positive to negative in several cases (e.g., P8–P13), suggesting a marked reduction in genotoxic potential. Overall, these findings confirm that the photocatalytic degradation of TC using the optimized $MgIn_2S_4/WO_3$ heterostructure not only achieves nearly complete structural breakdown but also substantially reduces the toxicity of resulting intermediates [77]. Although trace residuals of certain partially oxidized species persist temporarily, extended reaction time promotes their further oxidation and mineralization, ensuring environmentally benign effluents.

3.8. DFT cancelation

To rationalize the experimentally observed transformation routes of TC and to pinpoint the most labile sites under photocatalytic conditions, we performed single-molecule DFT analyses (DMol^3/PBE–GGA, DNP basis). Fig. 7a shows the electrostatic potential (ESP) mapped on the 0.001 e·bohr^3 isosurface. A distinct polarity emerges across the TC scaffold: electron-deficient domains (warm colors) concentrate around the dimethylamino substituent on ring D and adjacent carbonyls, whereas electron-rich pockets (cool colors) populate the phenolic/enolic oxygens on rings A–C. This polarization suggests that holes (h^+) and strongly oxidizing •OH radicals will preferentially attack the high-potential carbonyl/amine region, while superoxide ($\bullet O_2$) is more likely to add to, or abstract from, the electron-rich phenolic/enolic sites [78].

Frontier-orbital distributions (Fig. 7b and c) further localize the electronic activity. The HOMO (E = 0.1668 eV) is concentrated on the conjugated phenolic ring and the enol diketone motif, indicating that these π-rich centers are the primary electron donors and will be most susceptible to electrophilic oxidation by h^+/•OH. In contrast, the LUMO (E =0.1791 eV) extends over the amide/carbonyl domain and the dimethylamino terminus, consistent with these sites acting as first recipients of incoming electrons (i.e., prone to nucleophilic addition by $\bullet O_2^-$ or reduction). The HOMO–LUMO spatial separation supports intramolecular charge transfer upon excitation and aligns with the stepwise oxidation/reduction sequence deduced from LC–MS [79].

Fukui–function analysis provides quantitative site selectivity (Figs. 7d–7e). Atoms with large f^- values (electrophilic-attack susceptibility) include O6, O7, O8 and selected hydrogens (H45, H47), marking the enolic and phenolic oxygens as the preferred targets of h^+/•OH. This prediction matches the early hydroxylation/dehydrogenation and C–N/C–C bond activation observed in Path I of the degradation scheme. Atoms with large f^+ (nucleophilic-attack susceptibility) cluster around O3, O5, C22, C31, i.e., the carbonyl/quinone-like fragments that can accept electron density from $\bullet O_2^-$, facilitating reductive steps and ring-opening reactions seen in Paths II–III. Non-negligible f^0 values (radical susceptibility) on O3/O5/C18/C22 indicate sites where H-abstraction and radical rearrangements can proceed, providing plausible channels to the mid-mass intermediates (P6–P11). Charge-density difference (CDD) values in the same table emphasize the role of the tertiary amine (N9) and neighboring carbonyls as electron-withdrawing centers (largest positive CDD), which renders the dimethylamino side chain vulnerable to oxidative dealkylation/demethylation—the experimentally observed first step (P1 → P2 → P3) [80]. Concomitantly, the electron-rich phenolic oxygens (negative CDD together with high f) rationalize facile •OH attack, triggering ring hydroxylation and subsequent C–C/C–O bond cleavage that leads to ring-opening (P7–P9) and, ultimately, to low-molecular-weight fragments (P12–P13) and mineralization products (CO_2, H_2O, NH_4^+). Overall, the ESP polarity, frontier-orbital topology, Fukui functions, and CDD collectively provide a consistent atomistic picture: (i) h^+/•OH initiate oxidation at the enolic/phenolic domain and the dimethylamino/carbonyl cluster, (ii) $\bullet O_2$ engages the carbonyl/quinone centers to promote reductive additions and ring scission, and (iii) radical pathways (high f^0) assist in reorganizing the skeleton toward smaller, less toxic fragments [81]. These DFT-derived reactivity maps therefore corroborate the experimentally deduced pathways and explain why the *Z*-scheme $MgIn_2S_4/WO_3$ system—capable of concurrently supplying highly oxidative holes (WO_3 VB, +3.14 eV) and strongly reducing electrons ($MgIn_2S_4$ CB, 0.65 eV)—efficiently drives the selective bond activations needed for deep TC mineralization.

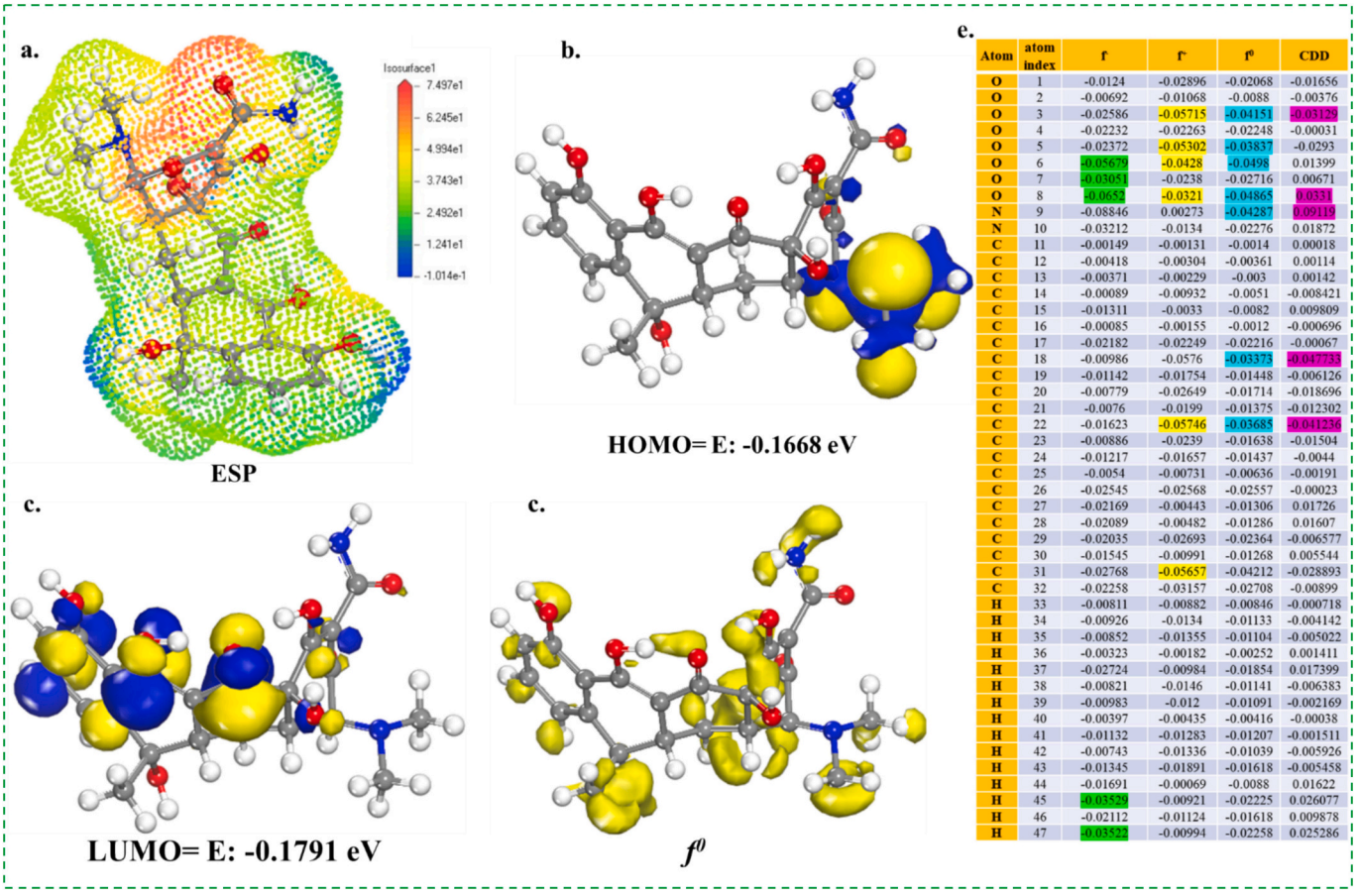

e.

Atom	atom index	f⁺	f⁻	f⁰	CDD
O	1	-0.0124	-0.02896	-0.02068	-0.01656
O	2	-0.00692	-0.01068	-0.0088	-0.00376
O	3	-0.02586	-0.05715	-0.04151	-0.03129
O	4	-0.02232	-0.02263	-0.02248	-0.00031
O	5	-0.02372	-0.05302	-0.03837	-0.0293
O	6	-0.05679	-0.0428	-0.0498	0.01399
O	7	-0.03051	-0.0238	-0.02716	0.00671
O	8	-0.0652	-0.0321	-0.04865	0.0331
N	9	-0.08846	0.00273	-0.04287	0.09119
N	10	-0.03212	-0.0134	-0.02276	0.01872
C	11	-0.00149	-0.00131	-0.0014	0.00018
C	12	-0.00418	-0.00304	-0.00361	0.00114
C	13	-0.00371	-0.00229	-0.003	0.00142
C	14	-0.00089	-0.00932	-0.0051	-0.008421
C	15	-0.01311	-0.0033	-0.0082	0.009809
C	16	-0.00085	-0.00155	-0.0012	-0.000696
C	17	-0.02182	-0.02249	-0.02216	-0.00067
C	18	-0.00986	-0.0576	-0.03373	-0.047733
C	19	-0.01142	-0.01754	-0.01448	-0.006126
C	20	-0.00779	-0.02649	-0.01714	-0.018696
C	21	-0.0076	-0.0199	-0.01375	-0.012302
C	22	-0.01623	-0.05746	-0.03685	-0.041236
C	23	-0.00886	-0.0239	-0.01638	-0.01504
C	24	-0.01217	-0.01657	-0.01437	-0.0044
C	25	-0.0054	-0.00731	-0.00636	-0.00191
C	26	-0.02545	-0.02568	-0.02557	-0.00023
C	27	-0.02169	-0.00443	-0.01306	0.01726
C	28	-0.02089	-0.00482	-0.01286	0.01607
C	29	-0.02035	-0.02693	-0.02364	-0.006577
C	30	-0.01545	-0.00991	-0.01268	0.005544
C	31	-0.02768	-0.05657	-0.04212	-0.028893
C	32	-0.02258	-0.03157	-0.02708	-0.00899
H	33	-0.00811	-0.00882	-0.00846	-0.000718
H	34	-0.00926	-0.0134	-0.01133	-0.004142
H	35	-0.00852	-0.01355	-0.01104	-0.005022
H	36	-0.00323	-0.00182	-0.00252	0.001411
H	37	-0.02724	-0.00984	-0.01854	0.017399
H	38	-0.00821	-0.0146	-0.01141	-0.006383
H	39	-0.00983	-0.012	-0.01091	-0.002169
H	40	-0.00397	-0.00435	-0.00416	-0.00038
H	41	-0.01132	-0.01283	-0.01207	-0.001511
H	42	-0.00743	-0.01336	-0.01039	-0.005926
H	43	-0.01345	-0.01891	-0.01618	-0.005458
H	44	-0.01691	-0.00069	-0.0088	0.01622
H	45	-0.03529	-0.00921	-0.02225	0.026077
H	46	-0.02112	-0.01124	-0.01618	0.009878
H	47	-0.03522	-0.00994	-0.02258	0.025286

Fig. 7. (a) ESP map, (b) HOMO, (c) LUMO, (d) Fukui function isosurface, and (e) condensed Fukui indices and CDD values of TC, illustrating charge distribution and reactive sites governing its photocatalytic oxidation and reduction pathways.

3.9. Comparison study

Table S5 compares the photocatalytic TC degradation performance of the $MgIn_2S_4/WO_3$ heterojunction developed in this work with representative photocatalysts previously reported in the literature under broadly comparable visible-light conditions. Overall, most reported systems achieve ~72.2–87.2% TC removal within 60–120 min, with apparent pseudo-first-order rate constants typically in the range of 0.0108–0.0333 min^{1}. In contrast, the $MgIn_2S_4/WO_3$ photocatalyst exhibits a markedly higher removal efficiency of 97.69% with a corresponding kinetic constant of 0.0539 min^{1} at an initial TC concentration of 26.95 mg L^{1} and a reaction time of 64.5 min, indicating a faster degradation rate and deeper conversion under a relatively demanding pollutant loading. It should be noted that direct comparison of removal percentage across studies is inherently influenced by experimental conditions, including initial TC concentration (10–50 mg L^{1}), catalyst dosage (0.2–0.68 g L^{1}), irradiation intensity/spectrum, and reactor configuration. Therefore, the kinetic constant provides a more informative normalization of reaction speed. From this perspective, the $MgIn_2S_4/WO_3$ system ranks among the higher-activity photocatalysts in the comparison set, outperforming most g-C_3N_4-based and mixed-oxide/sulfide composites and approaching high-rate systems reported under lower TC concentrations and/or specific plasmonic architectures. The combination of high degradation efficiency within a short irradiation time and an elevated kinetic constant supports the effectiveness of the $MgIn_2S_4/WO_3$ interface for TC abatement and highlights its competitiveness among state-of-the-art photocatalysts reported for tetracycline removal.

4. Conclusions and future perspectives

In this work, a direct *Z*-scheme $MgIn_2S_4/WO_3$ heterojunction was rationally constructed to couple efficient charge separation with dual environmental functionality. Beyond demonstrating strong photocatalytic activity, the integrated mechanistic analyses (radical identification, interfacial charge-transfer interpretation, and theoretical verification) clarify how interfacial band alignment and internal electric-field effects can be leveraged to preserve high redox capability in composite systems. Importantly, the study provides a reusable design rationale for developing dual-functional photocatalysts that simultaneously address antibiotic abatement and solar-driven carbon utilization within a single materials platform. Future efforts should prioritize catalyst immobilization and continuous-flow operation in realistic sunlight-driven reactors, alongside deeper evaluation of long-term stability and CO_2 conversion selectivity to accelerate practical translation. For next steps, future work should (i) optimize the heterointerface through controlled facet exposure, defect/vacancy regulation, and compositional tuning to further enhance charge-transport kinetics and Z-scheme efficiency; (ii) transition from powder suspensions to practical configurations by catalyst immobilization on conductive/porous supports and validation in continuous-flow, sunlight-driven reactors; and (iii) broaden durability and applicability assessments by testing in real water matrices (e.g., surface water, wastewater effluent) containing competing ions and natural organic matter, alongside extended-cycle stability studies and post-reaction structural/chemical diagnostics. In parallel, deeper investigation of CO_2 conversion pathways—quantifying product selectivity, carbon balance, and quantum efficiency under standardized conditions—will be essential to clarify scalability and

guide reactor-level integration.

CRediT authorship contribution statement

Yinghe Yang: Data curation, Formal analysis, Funding acquisition, Investigation, Software, Validation, Writing – review & editing. **Ali B.M. Ali:** Data curation, Formal analysis, Funding acquisition, Investigation, Software, Validation, Writing – review & editing. **Shatha A. Aldaghfag:** Data curation, Formal analysis, Funding acquisition, Investigation, Software, Validation, Writing – review & editing. **Haitao Lin:** Data curation, Formal analysis, Funding acquisition, Investigation, Software, Validation, Writing – review & editing. **Hedi Elmonser:** Data curation, Formal analysis, Funding acquisition, Investigation, Software, Validation, Writing – review & editing. **Ibrahm Mahariq:** Data curation, Formal analysis, Funding acquisition, Investigation, Software, Validation, Writing – review & editing. **Bakhodir Saydullaev:** Data curation, Formal analysis, Funding acquisition, Investigation, Software, Validation, Writing – review & editing. **Mukhtorjon Karimov:** Data curation, Formal analysis, Funding acquisition, Investigation, Software, Validation, Writing – review & editing. **Miyribek Seytnazarov:** Data curation, Formal analysis, Funding acquisition, Investigation, Software, Validation, Writing – review & editing. **Reda A. Haggam:** Data curation, Formal analysis, Funding acquisition, Investigation, Software, Validation, Writing – review & editing.

Declaration of competing interest

The authors declare that they have no known competing financial interests or personal relationships that could have appeared to influence the work reported in this paper.

Acknowledgments

The author extends the appreciation to the Deanship of Postgraduate Studies and Scientific Research at Majmaah University for funding this research work through the project number (ER-2025-2093). The authors also express their gratitude to Princess Nourah bint Abdulrahman University Researchers Supporting Project number (PNURSP2026R81), Princess Nourah bint Abdulrahman University, Riyadh, Saudi Arabia.

Appendix A. Supplementary data

Supplementary data to this article can be found online at https://doi.org/10.1016/j.seppur.2026.136908.

Data availability

No data was used for the research described in the article.

References

[1] L. Yang, R.P. Sivasankaran, M.K. Song, A.U. Pawar, D.K. Lee, Y.S. Kang, Highly selective solar CO2 conversion into formic acid in nickel-perylene-C3N4 semiconductor photocatalyst, Adv. Energy Mater. 15 (2025) 2402798.
[2] Z. Tabani, H. Maghsoudi, A. Fathollahi Zonouz, High electrochemical stability of polyvinylidene fluoride (PVDF) porous membranes using phase inversion methods for lithium-ion batteries, J. Solid State Electrochem. 25 (2021) 651–657.
[3] X. Li, Z. Wang, Y. Zhang, W. Zhang, H. Zhang, P. Liu, T. Lei, Hydrogen-rich gas formation from catalytic pyrolysis of biomass tar by aluminum dross coupled HZSM-5 co-loaded Ni-Fe bimetallic catalysts: influence of co-carrier characteristics, J. Environ. Manag. 389 (2025) 126016.
[4] J. Qin, J. Xie, Y. Zheng, J. Yang, H. Yamashita, J. Shang, Y. Hu, Construction of co-MOF-derivative modified TiO2 photocatalyst with uniform co site: a synergistic route for CO2 reduction and waste polypropylene plastic treatment, J. Environ. Chem. Eng. 13 (2025) 116767.
[5] A.M. Sadanandan, M. Fawaz, N.P. Dharmarajan, M. Huš, G. Singh, C.I. Sathish, B. Likozar, Z. Li, A.M. Ruban, C.-H. Jeon, J.-H. Yang, P. Kumar, A. Vinu, Mesoporous C-doped C3N5 as a superior photocatalyst for CO2 reduction, Appl. Catal. B Environ. Energy 362 (2025) 124701.
[6] L. Guo, W. Chen, C. Wang, B. Dong, Application of electrochemically assisted synthesis of MOFs-derived phosphides as catalyst for CH4-CO2 reforming, Int. J. Electrochem. Sci. 18 (2023) 26–32.
[7] P. Cao, M. Long, X. Zheng, C. Zhou, Y. Chen, B.E. Rittmann, Selective regulation of product generation from CO2 hydrogenation on pd-based catalysts: a critical review from a pathway perspective, Energy Environ. Sustain. 1 (2025) 100020.
[8] P.A. Taksal, S. Arasavilli, B.K. Das, K. Ray, S. Chowdhury, J. Bhattacharya, Green graphitic-carbon bridged Ag2S/g-C3N4 S-scheme photocatalyst for tetracycline degradation in water with antimicrobial activity: from synthesis to commercialization prospect, Sep. Purif. Technol. 361 (2025) 131610.
[9] L. Shi, G. Wang, K. Tang, C. Yang, J. Yang, S. Xiong, A. Tang, X. Zhang, Montmorillonite improved the tetracycline degradation performance of Br-doped BiOCl photocatalyst, Chem. Eng. Sci. 318 (2025) 122188.
[10] A. Moridi, S. Sabbaghi, J. Rasouli, K. Rasouli, S.A. Hashemi, W.-H. Chiang, S. M. Mousavi, Removal of cefixime from wastewater using a superb nZVI/copper slag nanocomposite: optimization and characterization, Water 15 (2023) 1819.
[11] M. Malekshahi, S. Sabbaghi, K. Rasouli, Preparation of α-alumina/γ-alumina/γ-alumina-titania ceramic composite membrane for chloride ion removal, Mater. Chem. Phys. 287 (2022) 126218.
[12] W. Pan, Z.-H. Zhu, Y.-S. Zhao, L. Jie, Z.-G. Zhang, G.-X. Li, T. Yu, Z.-Z. Han, Y.-Z. Long, G.-F. Yu, Chitosan/PEO@Eu-MOF nanofiber membrane-based test strip for visual detection of tetracycline with smartphone-assisted analysis, Chem. Eng. J. 520 (2025) 165936.
[13] J.Y. Lu, Z.Q. Bu, Y.Q. Lei, D. Wang, B. He, J. Wang, W.T. Huang, Facile microwave-assisted synthesis of Sb2O3-CuO nanocomposites for catalytic degradation of p-nitrophenol, J. Mol. Liq. 409 (2024) 125503.
[14] Z. Chen, J. Li, J. Zhang, H. Wang, Y. Zeng, F. Wang, P. Huang, X. Chen, L. Ge, R. A. Dahlgren, H. Gao, X. Huang, A highly efficient and recyclable living biocatalyst using Shewanella@polydopamine@NH2-doped carbon dot biohybrids and polypyrrole immobilized melamine foam for microbial-photoreduction of Cr(VI), J. Clean. Prod. 435 (2024) 140497.
[15] K. Rasouli, J. Rasouli, M.S. Mohtaram, S. Sabbaghi, H. Kamyab, H. Moradi, S. Chelliapan, Biomass-derived activated carbon nanocomposites for cleaner production: a review on aspects of photocatalytic pollutant degradation, J. Clean. Prod. 419 (2023) 138181.
[16] J. Wang, J. Zhang, G. Cheng, K. Zhang, X. Liu, Performance and mechanism of tetracycline removal by peroxymonosulfate-assisted double Z-scheme LaFeO3/g-C3N4/ZnO heterojunction under visible light drive, Environ. Technol. Innovation 39 (2025) 104302.
[17] M. Akbari, J. Rasouli, K. Rasouli, S. Ghaedi, M. Mohammadi, H. Rajabi, S. Sabbaghi, MXene-based composite photocatalysts for efficient degradation of antibiotics in wastewater, Sci. Rep. 14 (2024) 31498.
[18] R. Li, B. Wang, Y. Zhao, N. Zhang, X. Zhao, Z. Gao, H. Guo, H. Wang, In-situ growth of WO3/Bi2WO6 heterojunctions on carbon fiber cloth: design, morphology modulation and photocatalytic performance, J. Environ. Chem. Eng. 13 (2025) 118926.
[19] K. Rasouli, A. Alamdari, S. Sabbaghi, Ultrasonic-assisted synthesis of α-Fe2O3@TiO2 photocatalyst: optimization of effective factors in the fabrication of photocatalyst and removal of non-biodegradable cefixime via response surface methodology-central composite design, Sep. Purif. Technol. 307 (2023) 122799.
[20] J. Zhao, A.B.M. Ali, A.A.H. Kadhum, H. Lin, A.S. Abdelhameed, A.M. Alanazi, I. Mahariq, E. Khudoynazarov, D. Jumanazarov, F. Atamurotov, Boosting photocatalytic H2O2 production and non-biodegradable ofloxacin removal via a novel Ti3C2 MXene nanosheet-supported BiVO4/InVO4 Z-scheme heterojunction: optimization and mechanism insights, J. Water Process Eng. 74 (2025) 107722.
[21] Q. Liu, S. Dong, H. Jin, S. Ke, L. Luo, T. Huang, Preparation of MgIn2S4/g-C3N4 for enhanced ranitidine photocatalytic degradation activity via Z-scheme electron transfer, J. Environ. Chem. Eng. 11 (2023) 111568.
[22] M.H. Abdallah, A.B.M. Ali, Y.M. Fahmy, S.A. Aldaghfag, N.S. Alsaiari, M. Karimov, E. Davletov, D. Raupov, I. Mahariq, R.A. Haggam, Switching charge transfer of Ce2Sn2O7–SiW9Co3 from type-II to Z-scheme for efficient visible-light-driven hydrogen evolution and tetracycline degradation, J. Water Process Eng. 81 (2026) 109332.
[23] Y. Yang, A.B.M. Ali, Y.M. Fahmy, P.K. Singh, A. Amari, H. Lin, F. Jalilov, M. Karimov, E. Khudoynazarov, I. Mahariq, R.A. Haggam, Synthesis of a novel Ti3C2 MXene–based nanocomposite for photocatalytic wastewater treatment and CO2 conversion: DFT analysis, mechanistic insights, and process optimization, Sep. Purif. Technol. 385 (2026) 136291.
[24] Y. Wu, S. Gong, L. Chen, P. Yang, Preparation of n-n type ZnFe2O4/WO3 heterojunction photocatalyst and study on its high-efficiency photocatalytic reduction performance for U(VI), Surf. Interfaces 71 (2025) 106914.
[25] A. Rong, Q. Zhao, H. Shi, X. Cai, H. Zhu, C. Chen, X. Zhou, G. Yan, L. Mao, Fabrication of CoTiO3/MgIn2S4 S–scheme heterojunctions with efficient charge separation to enhance the photocatalytic activities of hydrogen generation and formaldehyde removal, Sep. Purif. Technol. 356 (2025) 130010.
[26] X.A. Dong, W. Dai, C. Yang, X. Li, R. Tang, X. Shi, Localized strain induced carrier separation and filtering in S-scheme MgIn2S4@CdS heterojunction for boosting selective CO2 photoreduction, Chem. Eng. J. 524 (2025) 169282.
[27] M.S. Mohtaram, S. Sabbaghi, J. Rasouli, K. Rasouli, Photocatalytic degradation of tetracycline using a novel WO3–ZnO/AC under visible light irradiation: optimization of effective factors by RSM-CCD, Environ. Pollut. 347 (2024) 123746.
[28] H. Yu, D.T. Hoang, H.S. Kim, H. Lee, In situ study of CdS/WO3 and CdS/SnO2 heterostructures: comparison of photocatalytic activity behavior, J. Mater. Chem. A 13 (2025) 6049–6058.

[29] M. Cheng, H. Li, Z. Wu, Z. Yu, X. Tao, L. Huang, Synergistic effects of CQDs and oxygen vacancies on CeO2 photocatalyst for efficient photocatalytic nitrogen fixation, Sep. Purif. Technol. 354 (2025) 129299.
[30] M. Gunawan, M. Priest, D. Gunawan, S. Nie, A. Satriyatama, J. Vongsvivut, Z. Hameiri, Q. Zhang, S. Zhou, R. Amal, Differentiating the role of Ni and Fe in NiFeOx co-catalyzed BiVO4 photoanode for water oxidation, Energy Environ. Sustain. 1 (2025) 100019.
[31] P.J. Mafa, M.E. Malefane, F. Opoku, A.O. Oladipo, G. Mamba, T.L. Yusuf, J.F. Nure, S.L. Lebelo, D. Liu, J. Gui, B.B. Mamba, A.T. Kuvarega, Dual charge transfer mechanisms in intimately bonded S-scheme heterojunction photocatalyst with expeditious activity toward environmental remediation, Adv. Sustainable Syst. 9 (2025) 2401070.
[32] L. Wang, J. Zhao, Organic/inorganic composite S-scheme photocatalyst with enhanced light absorption and H2O2-production activity, J. Mater. Sci. Technol. 241 (2026) 18–20.
[33] Y. Wei, Z. Su, H. Gu, K. Wang, J. Hu, L. Wang, CdZnS Nanoparticles Supported on an Ultrathin Cu Metal–Organic Layer as an S-Scheme Photocatalyst for Hydrogen Production and Pollutant Degradation, ACS Appl. Nano Mater.42 (2025)20387-20396.
[34] Y. Lu, Y. Zhao, S. Wang, B. Hu, Exploring charge-transfer of 2D borophene in carbon nitride: boosting uranium photoreduction, Desalination 619 (2026) 119488.
[35] S. Karami, A. Heidarinasab, H. Ahmad Panahi, M. Ghasemian, Modification of tungsten trioxide with Polyamidoamine dendrimer: a thermosensitive nanocarrier for near-infrared laser triggered delivery of docetaxel, J. Polym. Environ. 33 (2025) 12–28.
[36] A. Rong, H. Shi, Q. Zhao, H. Zhu, H. Wang, G. Yan, Boosted photocatalytic performance of hydrogen evolution and formaldehyde degradation with a S-scheme PMo12/MgIn2S4 heterojunction, Sep. Purif. Technol. 348 (2024) 127782.
[37] L. Ma, S. Liu, J. Xu, N. Zhao, S. Li, W. Jiang, Z. Pan, B. Yang, Y. Liu, B. Lai, Synergistic integration of oxygen vacancy enrichment and Z-scheme heterojunction in novel Bi4O7/TiO2-x photocatalyst for enhanced tetracycline degradation in wastewater, J. Environ. Manag. 391 (2025) 126674.
[38] X. Sun, H. Yang, J. Xie, G. Teng, J. He, Z. Zhao, C. Zhang, A photocatalyst combined of copper doped ZnO and graphdiyne (cu/ZnO@GDY) for photocatalytic degradation of tetracycline: mechanism and application, Water Res. 278 (2025) 123345.
[39] Y. Pajouhan, S. Sabbaghi, K. Rasouli, J. Rasouli, W. Dastyar, E. Andiroglu, Enhanced photocatalytic degradation of tetracycline using α-Fe2O3@TiO2-impregnated Mxene photocatalyst: mechanism and optimization of process via RSM and ANN, Process. Saf. Environ. Prot. 190 (2024) 1149–1163.
[40] J. Huang, A.B.M. Ali, A. Abdulrahman, A.A.H. Kadhum, S. Samad, H. Osman, M. A. Diab, M. Karimov, H.A. El-Sabban, E. Saitov, Constructing a novel Z-scheme Fe2O3/ZnIn2S4@Bi2WO6 photocatalyst for boosting removal of non-biodegradable ciprofloxacin and long-term stable CO2 conversion, J. Water Process Eng. 72 (2025) 107632.
[41] T. Thiruppathiraja, B. Rhimi, N. Zhang, M. Zhou, W. Shi, Z. Jiang, Theoretical investigations of hydroxyl-functionalized iron-doped phthalocyanine photocatalyst for efficient CO2 reduction to methanol and methane, Chem. Eng. Sci. 305 (2025) 121121.
[42] S. Sharma, P. Dhull, R. Kumar, A. Sudhaik, P. Raizada, Q.V. Le, A.A. Parwaz Khan, P. Singh, T. Kamal, K.A. Alzahrani, Recent updates on a Cs3Bi2Br9-based heterojunction photocatalyst for selective CO2 conversion into (CO/CH4) products, J. Ind. Eng. Chem. 148 (2025) 724–741.
[43] J. Tang, M. He, B. Zhang, K. Zhong, Z. Yang, Z. Wang, X. Zhu, H. Li, J. Yang, H. Xu, Enhancing photocatalytic CO2 reduction by fabricating intimate contact interfacial of SnIn4S8/Co3O4 2D-2D heterojunction photocatalyst, J. Colloid Interface Sci. 694 (2025) 137711.
[44] M.S. Sulabha, A. V, J.A. B.M, Hydroxyl functionalised 2D/2D Ti2CTx MXene @ g-C3N4 photocatalyst confer selectivity for CO2 reduction to ethanol, Appl. Surf. Sci. 686 (2025) 162104.
[45] H. Zhang, X. Han, J. Zhu, S. Lou, P. Song, Y.J. Dappe, Z. Yang, Y. Wang, J. Zhu, A metal-free boron carbon nitride (BCN) photocatalyst for enhanced CO2-to-CH4 conversion by surface electronic tuning, Sol. RRL 9 (2025) 2500037.
[46] J. Rasouli, A. Zandifar, K. Rasouli, S. Sabbaghi, F. Esmaeilzadeh, M. Shah, K. B. Ansari, High-efficiency ternary CeO2/WO3/AC photocatalyst supported by biomass waste-derived activated carbon for efficient doxycycline photodegradation: optimization of synthesis conditions and operational parameters, Mater. Res. Bull. 178 (2024) 112874.
[47] M. Gonbadi, S. Sabbaghi, J. Rasouli, K. Rasouli, R. Saboori, M. Narimani, Green synthesis of ZnO nanoparticles for spent caustic recovery: adsorbent characterization and process optimization using I-optimal method, Inorg. Chem. Commun. 158 (2023) 111460.
[48] P. Sarani, S. Sabbaghi, K. Rasouli, N.S. Mirbagheri, J. Rasouli, Optimization of chloride ion removal from drinking water using graphene oxide modified with AgNO3 via CCD-based RSM method, Inorg. Chem. Commun. 160 (2024) 111930.
[49] J. Rasouli, M. Binazadeh, S. Sabbaghi, Synthesis of a novel biomass waste-based photocatalyst for degradation of high concentration organic pollutants under visible light: optimization of synthesis condition and operational parameters via RSM-CCD, Surf. Interfaces 49 (2024) 104400.
[50] S.M. Mousavi, M.S. Mohtaram, K. Rasouli, S. Mohtaram, H. Rajabi, S. Sabbaghi, Efficient visible-light-driven photocatalytic degradation of antibiotics in water by MXene-derived TiO2-supported SiO2/Ti3C2 composites: optimisation, mechanism and toxicity evaluation, Environ. Pollut. 367 (2025) 125624.
[51] L. Hongtanee, K. Wannakan, S. Nonthing, A. Panchakeaw, S. Nijpanich, S. Nanan, Solvothermally grown ZnO/BiOCl photocatalyst for solar-light-responsive degradation of tetracycline antibiotic, OpenNano 25 (2025) 100253.
[52] C. Li, Y. Cai, J. Wu, L. Li, S.-S. Xia, X. Wang, R. Jia, Z. Chen, C.-C. Jin, W. Wang, R. Wang, N. Zhang, High-concentration single-atom Zn-doped porous tubular g-C3N4: a superior photocatalyst for tetracycline hydrochloride degradation and bacterial sterilization, Rare Metals 44 (2025) 4756–4766.
[53] C. Zhang, S. Hu, W. Cui, S. Li, L. Tian, X. Yuan, W. Tariq, K. Yao, Y. Zhi, T. Hu, S. Shan, Integrating photocatalytic hydrogen evolution with antibiotic degradation over a dual Z-scheme heterojunction, Chem. Eng. J. 510 (2025) 160317.
[54] W. Li, W. Wang, C. Wang, Y. Huang, W. Liu, W. Zhao, Z. Xu, G. Li, T. An, Synergy of dual dopants and nitrogen defects in graphitic carbon nitride for boosting sustainable photocatalytic inactivation efficiency towards antibiotic-resistant bacteria, Chem. Eng. J. 507 (2025) 160404.
[55] J. Choi, J. Kim, S. Seo, H. Ko, S. Lee, S. Joung, M. Kim, H. Lee, Hydroxyl radical-exclusive Z-scheme photocatalyst for fast and complete disinfection of antibiotic-resistant bacteria-contaminated water, Chem. Eng. J. 521 (2025) 166363.
[56] M. Fang, N. Li, Y. Han, H. Gao, F. Li, J. Wang, J. Wang, Y. Xiang, L. Zhang, D. Wang, Br self-doping enhances the piezo-photocatalysis of BiOBr for efficient CO2 reduction and antibiotic degradation, Chem. Eng. J. 524 (2025) 169525.
[57] H. Deng, Y. Wu, L. Li, X. Jiang, P. Wang, K. Fang, J. Li, D. Hao, H. Zhu, Q. Wang, Q. Li, Synergistic mechanisms for efficient and safe antibiotic removal: effective adsorption and photocatalytic degradation using aerogels, Sep. Purif. Technol. 354 (2025) 129455.
[58] Z. Li, Y. Tong, M. Hassan, M. Lv, Y. Qiu, H. Li, X. Yang, Z. Gong, J. Niu, Employing lattice compression spin polarization electric field for boosting degradation of mixed antibiotics in wastewater, Sep. Purif. Technol. 354 (2025) 128922.
[59] F. Wei, M. Xin, Z. Kang, X. Chen, H. He, K. Ren, R. Song, H. Wang, G. Zeng, Highly efficient and stable photo-Fenton-like catalytic membrane based on yolk-Shell MOF-on-MOF nanostructures for broad-Spectrum antibiotic removal, Sep. Purif. Technol. 378 (2025) 134743.
[60] H. Tang, H.E.C. Yao, X. Wang, J. Zhou, W. Song, Z. Zhang, Boosted Antibiotic Elimination over 2D/2D Mesoporous CeO2/BiOCl S-Scheme Photocatalyst vol. 354, Separation and Purification Technology, 2025, p. 128977.
[61] J. Hong, J. Dong, X. Zhang, G. Liu, L. Li, B. Wang, M. Ji, H. Li, J. Xia, The synergistic effect of low concentration of peroxymonosulfate and visible light photocatalysis over FeOOH quantum dots/hollow g-C3N4 nanotubes S-scheme heterojunction for effectively antibiotics degradation, J. Environ. Chem. Eng. 13 (2025) 115777.
[62] S. Li, J. Hu, Photolytic and photocatalytic degradation of tetracycline: effect of humic acid on degradation kinetics and mechanisms, J. Hazard. Mater. 318 (2016) 134–144.
[63] D. Awfa, M. Ateia, M. Fujii, C. Yoshimura, Photocatalytic degradation of organic micropollutants: inhibition mechanisms by different fractions of natural organic matter, Water Res. 174 (2020) 115643.
[64] C.-H. Liao, S.-F. Kang, F.-A. Wu, Hydroxyl radical scavenging role of chloride and bicarbonate ions in the H2O2/UV process, Chemosphere 44 (2001) 1193–1200.
[65] G. Liu, S. Han, X. Zhang, W. Zheng, B. Han, F. Chen, H. Huang, Surface-iodine-grafting-induced local electric field drives charge separation of CdBiO2Br for excellent photocatalytic antibiotic degradation, Appl. Surf. Sci. 680 (2025) 161350.
[66] M. Boujelbene, A.B.M. Ali, K. Alsaikhan, A. BaQais, M.B.B. Hamida, A. Amari, Y. Yusupov, A. Abduvokhidov, E. Khudoynazarov, Enhanced photocatalytic performance for organic pollutants degradation and H2O2 production using a novel rGO-bridged bi_2MoO_6-$CoTiO_3$ Z-scheme composites: analytical characterization, mechanism and toxicity assessment, Surf. Interfaces 72 (2025) 107201.
[67] M.A. Diab, A.B.M. Ali, A. Abdulrahman, A. BaQais, M.I. Khan, A. Abduvokhidov, M. Karimov, O. Mukhitdinov, I. Mahariq, Design and synthesis of a novel Fe3O4/ZIF-67/CuCo2S4 composite for efficient ciprofloxacin and Ni2+ removal from wastewater: characterization and mechanistic insights, Surf. Interfaces 73 (2025) 107517.
[68] H.A. El-Sabban, A.B.M. Ali, T.M. Alhuzaymi, A.A.H. Kadhum, M. Hasan, M.A. Diab, Z. Atamuratova, E. Saitov, Y.G. Ko, Visible light-driven photocatalytic degradation of norfloxacin by biochar-supported Cs3Bi2I9-Bi2MoO6 Z-scheme composite: characterization, optimization, and toxicity assessment, J. Water Process Eng. 70 (2025) 107131.
[69] Z. Algarni, H.S. Sultan Aljibori, A. Amari, D.J. Jasim, M.A. Diab, H.A. El-Sabban, N. Elboughdiri, I. Abdullayeva, A.A.H. Kadhum, Charge separation by switching heterojunction system from type-II to S-scheme for enhanced photocatalytic activity: environmental detoxification and H2 production, Sep. Purif. Technol. 357 (2025) 130069.
[70] M. Boujelbene, A. Basem, N.S. Alsaiari, S.A. Aldaghfag, M.A. Ismail, W. Rajhi, S. Ibragimova, A. Abilkasimov, Z. Atamuratova, Solar-driven dual-functional Z-scheme ZnIn2S4–Sb2O3 supported on activated carbon for simultaneous H2 generation and norfloxacin degradation: mechanism, analytical characterization, and toxicity assessment, Surf. Interfaces 75 (2025) 107785.
[71] F. Meng, C. Qu, L. Wang, D. Yang, Y. Luo, Z. Zhao, Q. Ye, Efficient CO2-to-CO conversion by Ni-Fe bimetallic oxide quantum dots embed in graphitic carbon nitride nanosheets: a novel visible-light-driven Z-scheme photocatalyst, Sep. Purif. Technol. 366 (2025) 132858.
[72] J. Zou, L. Li, N. Tan, K. Zhang, L. Wang, Z. Chen, Construction of S-scheme heterojunction with interfacial chemical bonds for enhanced photocatalytic CO2 reduction, Appl. Surf. Sci. 719 (2026) 165001.
[73] Y. Zhang, W.H. Hassan, H. Osman, Z. Algarni, M.M. Alharbi, K. Zhang, S. Sabirov, D. Jumanazarov, I. Mahariq, Enhanced environmental detoxification and ammonia

production using a novel $CeVO_4/bi_4O_5I_2$ Z-type photocatalyst: mechanistic insights, DFT calculations, and toxicity assessment, Sep. Purif. Technol. 380 (2026) 135338.
[74] H. Zhang, Q. Ma, G. An, Y. Zhu, X. Sun, N. Kawazoe, G. Chen, Y. Yang, Development of ag/Ag2O/BiPO4/Bi2WO6/g-C3N4 Z-scheme photocatalyst for high-efficiency tetracycline removal: characterization, degradation pathway and toxicity assessments, Environ. Funct. Mater. (2025).
[75] N. Liu, Y. Zhang, P. Liu, Z. Cheng, L. Kang, R. Ma, J. Lu, Efficient piezo-photocatalytic degradation of aqueous tetracycline over porous carbon nitride with detoxification analysis, J. Environ. Chem. Eng. 13 (2025) 119733.
[76] M.H. Aziz, M. Latif, R.U. Hassan, T. Naeem, M. Asif, M. Alam, S.M. Ali, Q. Zeng, Photocatalytic breakdown of tetracycline via Z-scheme BiFeO3/ag/Cr2O3 nanocomposite under visible light irradiation: degradation mechanism, toxicity evaluation and antibacterial activity, Surf. Interfaces 61 (2025) 106151.
[77] M.H. Aziz, M. Fatima, A.S. Farooq, N. Kanwal, Q. Huang, A novel Z-scheme visible light driven photocatalyst AgZnFe2O4/V2O5/RGO for boosting the degradation of tetracycline antibiotics: gated recurrent unit (GRU) and response surface methodology (RSM) models, toxicity and degradation pathways, Surf. Interfaces 56 (2025) 105606.
[78] X. He, X. Yang, Y. Li, J. Yang, Y. Wang, S. Cui, Visible light-induced photocatalytic degradation of tetracycline based on cu/CDs/$BiVO_4$ ternary core-shell composite: DFT calculations and mechanism, Appl. Catal. A Gen. 699 (2025) 120256.
[79] Z. Li, R. Zhang, M. Xu, J. He, Y. Liu, D. Chen, D. Li, Modification of bismuth-rich to synthesize floral spherical Z-type heterojunction CoAl2O4/Bi4O5Br2 photocatalysts for photocatalytic degradation of tetracycline: DFT calculations, toxicity assessment, J. Alloys Compd. 1010 (2025) 177864.
[80] Q. Ni, H. Shao, Y. Zhang, X. Ke, W. Liu, How to enhance photocatalytic efficiency for tetracycline degradation in natural aquatic environments using oxygen-vacancy-modified BiOI/BiOBr composites: coupling DFT simulations with experiments, Environ. Res. 285 (2025) 122527.
[81] W.-Y. Li, J. Liu, Z.-R. Li, T.-T. Shen, J. Chen, Z.-Y. Hu, W.-B. Yu, Y. Li, B.-L. Su, Probing the deactivation and regeneration of ZnIn2S4 in photocatalytic degradation of tetracycline, J. Colloid Interface Sci. 694 (2025) 137700.